

AD_____

AWARD NUMBER: W81XWH-05-1-0221

TITLE: Development of an Automated Modality-Independent Elastographic Image Analysis System for Tumor Screening

PRINCIPAL INVESTIGATOR: Jao J. Ou
Michael I. Miga, Ph.D.

CONTRACTING ORGANIZATION: The Vanderbilt University
Nashville, Tennessee 37235-7749

REPORT DATE: February 2006

TYPE OF REPORT: Annual Summary

PREPARED FOR: U.S. Army Medical Research and Materiel Command
Fort Detrick, Maryland 21702-5012

DISTRIBUTION STATEMENT: Approved for Public Release;
Distribution Unlimited

The views, opinions and/or findings contained in this report are those of the author(s) and should not be construed as an official Department of the Army position, policy or decision unless so designated by other documentation.

REPORT DOCUMENTATION PAGE

Form Approved
OMB No. 0704-0188

Public reporting burden for this collection of information is estimated to average 1 hour per response, including the time for reviewing instructions, searching existing data sources, gathering and maintaining the data needed, and completing and reviewing this collection of information. Send comments regarding this burden estimate or any other aspect of this collection of information, including suggestions for reducing this burden to Department of Defense, Washington Headquarters Services, Directorate for Information Operations and Reports (0704-0188), 1215 Jefferson Davis Highway, Suite 1204, Arlington, VA 22202-4302. Respondents should be aware that notwithstanding any other provision of law, no person shall be subject to any penalty for failing to comply with a collection of information if it does not display a currently valid OMB control number. PLEASE DO NOT RETURN YOUR FORM TO THE ABOVE ADDRESS.

1. REPORT DATE (DD-MM-YYYY) 01-02-2006	2. REPORT TYPE Annual Summary	3. DATES COVERED (From - To) 26 Jan 2005 – 25 Jan 2006		
4. TITLE AND SUBTITLE Development of an Automated Modality-Independent Elastographic Image Analysis System for Tumor Screening		5a. CONTRACT NUMBER		
		5b. GRANT NUMBER W81XWH-05-1-0221		
		5c. PROGRAM ELEMENT NUMBER		
6. AUTHOR(S) Jao J. Ou and Michael I. Miga, Ph.D. E-Mail: jjo@alumni.duke.edu		5d. PROJECT NUMBER		
		5e. TASK NUMBER		
		5f. WORK UNIT NUMBER		
7. PERFORMING ORGANIZATION NAME(S) AND ADDRESS(ES) The Vanderbilt University Nashville, Tennessee 37235-7749		8. PERFORMING ORGANIZATION REPORT NUMBER		
9. SPONSORING / MONITORING AGENCY NAME(S) AND ADDRESS(ES) U.S. Army Medical Research and Materiel Command Fort Detrick, Maryland 21702-5012		10. SPONSOR/MONITOR'S ACRONYM(S)		
		11. SPONSOR/MONITOR'S REPORT NUMBER(S)		
12. DISTRIBUTION / AVAILABILITY STATEMENT Approved for Public Release; Distribution Unlimited				
13. SUPPLEMENTARY NOTES				
14. ABSTRACT The objective of this project is to further develop modality-independent elastography as a system that is able to reproducibly detect regions of increased stiffness within the breast based on pre- and post- compression input images of the anatomy. As stated in the proposal, the original specific aims are concerned with enhancement of the method, investigation of texture and statistical analyses for evaluating the success of the method, and engineering of a device that can generate proper forces on mock setups within current available clinical imaging systems. To date, progress on each of these aims has been made in handling increased computational complexity, developing and testing metrics for the evaluation of reconstructions, and the fabrication of a compression chamber tested on a tissue-like polymer phantom.				
elastography, breast cancer screening, image processing				
16. SECURITY CLASSIFICATION OF: a. REPORT U		17. LIMITATION OF ABSTRACT UU	18. NUMBER OF PAGES 49	19a. NAME OF RESPONSIBLE PERSON USAMRMC
b. ABSTRACT U				19b. TELEPHONE NUMBER (include area code)
c. THIS PAGE U				

Table of Contents

Introduction.....	4
Body.....	4
Key Research Accomplishments.....	11
Reportable Outcomes.....	11
Conclusions.....	11
References.....	12
Appendices.....	13

Introduction

An important initial screening step in the detection of breast cancer is the ability to identify select areas of atypical density that require further evaluation. Currently, mammography is the clinical standard for screening and provides useful but at times ambiguous information, which can necessitate further invasive workup of benign lesions. Alternative methods such as elastography have shown potential in enhancing the diagnostic process by providing information about the tissue composition [1, 2]. Modality-independent elastography (MIE) is a novel image processing technique that combines finite element models of soft-tissue deformation with measures of image similarity in order to reconstruct elastic property distributions throughout the tissue. The basic requirements for the method are two images of the tissue in different states of deformation (e.g. compression). MIE then updates the estimate of the material properties via a matching process between the two images. The final result is a map of the breast (or other tissue of interest) that reflects material inhomogeneity, such as in the case of a tumor mass that disrupts the surrounding structure of normal tissue. Because MIE works on probing the differences between images, it can be used to not only work in concert with more traditional screening techniques but also address a possible gap when those methods are unable to directly discern tissues of interest.

Body

As stated in the original proposal, three main aims of this project are to (1) expand and refine the current MIE technique to enhance its efficiency and capabilities, (2) to perform analyses on texture in input images and quantify statistical parameters capable of estimating and evaluating the success of elastographic reconstruction, and (3) to engineer a device that can accurately produce compressive forces necessary for phantom setups within current imaging systems, providing the basis for a future device that can be used in a clinical setting. In this past year, progress on all three aims has been made. The original specific aim and the relevant proposed work for each is listed below and addressed.

Specific Aim #1 stated: **“To expand and refine the current MIE technique to enhance its efficiency, as well as add new capabilities such as handling a full 3D or combined 2D/3D elastodynamic model for improved accuracy.”**

An improved framework is in progress utilizing parallel processing techniques. In order to accommodate the methodology of MIE in creating a Jacobian matrix fully sensitive to the discretization of the domain, a large number of solutions involving the finite element model and the subsequent image deformation are required. With the proposed increase in dimensionality, the implementation complexity quickly increases beyond the capabilities of the original MATLAB/FORTRAN/LAPACK design. Therefore, the Portable Extensible Toolkit for Scientific Computation (PETSc) toolkit [3,4] was selected to provide the necessary framework for developing sparse matrix system solvers and split the Jacobian formation process. A separate C/C++ routine has also been written to perform a Gauss-Newton optimization and interface with PETSc solver structures. A current typical iteration involves the solution of a matrix system of approximately 1e5 equations, repeated some 3000 times. Utilizing parallel design and a share of 100 CPUs on the Vanderbilt University Advanced Computing Center for Research and

Education cluster, this has been tested to be achieved on the order of 30 minutes, as opposed to original estimates on available sequential processing machines upwards of 5000 minutes. We note, however, that to effectively traverse the full multi-dimensional objective function space requires several (perhaps tens of) iterations, which underscores the high computational demand of the method.

We have preliminary work that demonstrates the new MIE framework in action, using a test case of simulated deformation based on clinical data. Figure 1 shows orthogonal cuts in the three cardinal anatomic planes for an image volume obtained from a CT scan of a human breast. Fibroglandular tissue can be visually inspected to provide contrast and structure from adipose and other tissue types. The test case involves the simulated implantation of a 2-cm spherical tumor at the center of the breast that is not visible within the intensity field of the image. Guided by a finite element mesh deformation using prescribed boundary displacements (designed to mimic a compression source as described in Specific Aim 3), a target image volume is created. Discretizations of the model and image domains are then used in the optimization loop to reconstruct the inclusion. Figure 2 shows surface renderings of the image volumes and the results of a reconstruction based on 3200 spatially distributed elasticity regions. The areas delineated to be the true tumor extent contain entities that the algorithm designated as having stiffer properties ($\sim 2x$). It may be initially seen to be an improper characterization given that the faux tumor was actually six times stiffer than the surrounding tissues. However, in this test case, the inexact partitioning of the mesh elements actually caused the algorithm to search for a tumor about 3 cm in size, leading to a compensatory decrease in elasticity contrast.

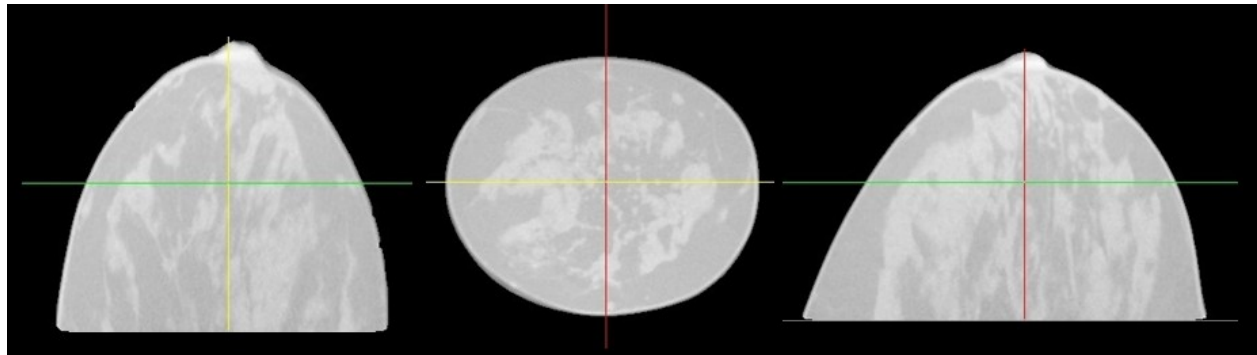


Figure 1. Orthogonal cuts of a CT breast scan used as the source image volume for simulation studies. From left to right: axial, coronal, and sagittal views as designated by the standard anatomical planes.

In order to further explain the relationship between discretization and reconstructed contrast, a partitioning of the mesh elements utilizing *a priori* knowledge of the location of the tumor was used to classify the tissue types, thereby reducing the reconstruction to two materials instead of the 3200. This reconstruction very favorably followed an objective function minimization to obtain an elasticity contrast of the inclusion being almost exactly six times stiffer as prescribed (see Figure 3 below). It is our current assertion that shaping the objective function by dynamically rearranging the spatial discretization of the model during the optimization can lead to improved elasticity contrast resolution, and studies are underway to address this issue.

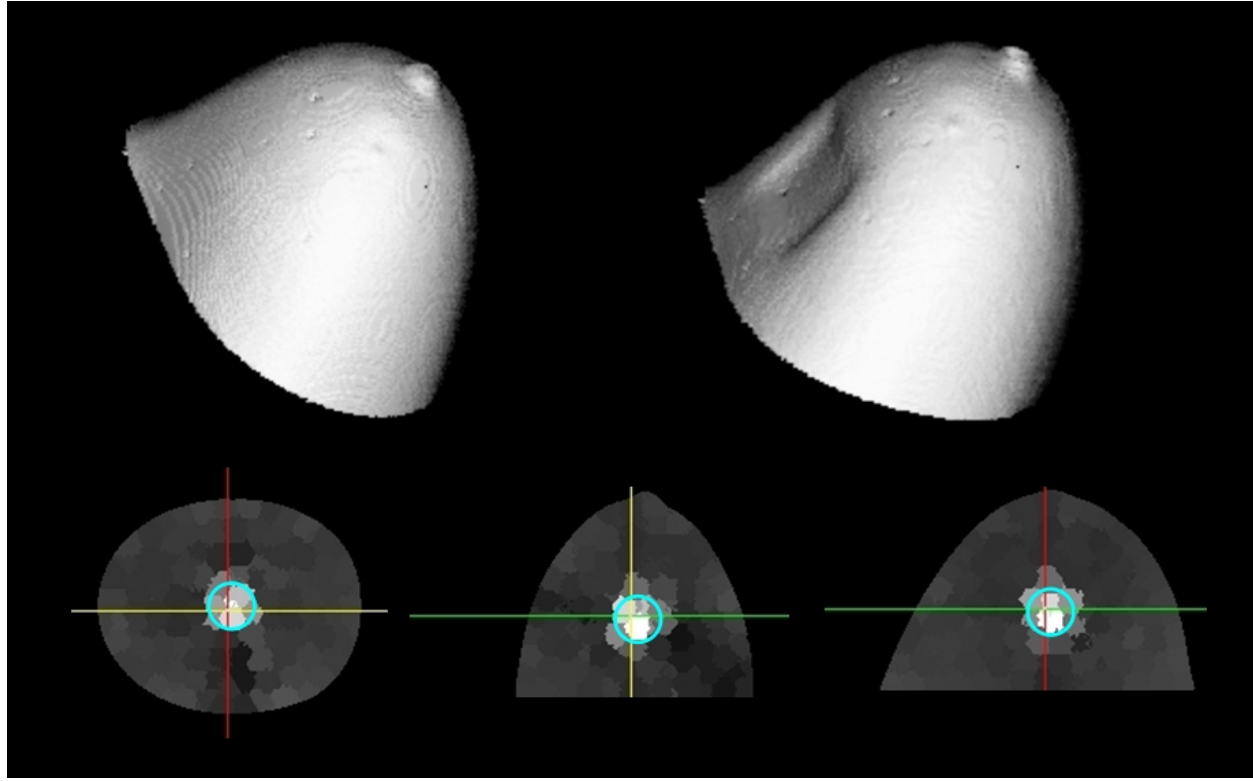
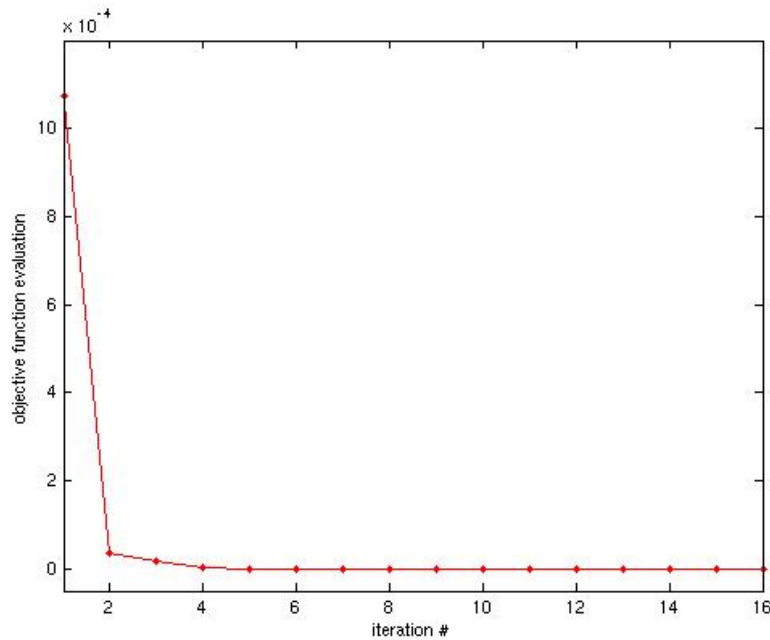


Figure 2. Top row: surface renderings in perspective of the breast image volume in both the native undeformed (left) and deformed (right) states. Bottom row: reconstruction mappings from a simulation experiment. Areas of high intensity reflect higher (stiffer) elasticity values; the boundary of the simulated tumor is overlaid by the circle.

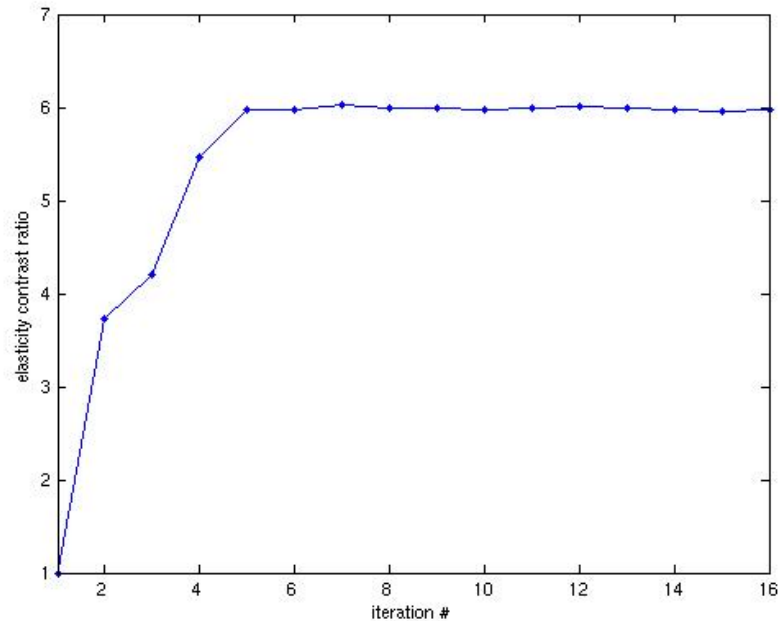
Proposed work involving the use of a combined 2D-3D model is under investigation but not completed at this time. It is hoped that reducing the scope of the problem by dimensionality will facilitate further analysis of the problem by alleviating the time and resource restrictions of the full implementation.

Specific Aim #2 stated: **“To perform texture analysis on input images in order to quantify a statistical parameter capable of estimating the success of elastographic reconstruction.”**

Texture analysis and noise tolerance testing has been performed with statistical quantification of reconstruction success. Our observations during the ongoing development and testing of the MIE method prompted questions concerning the quality of data necessary and sufficient to achieve satisfactory results (i.e., the fidelity of the reconstructed elasticity image). The primary inputs to the reconstruction method are the acquired images and the delineated boundary conditions on the domain. While it is clearly preferable to have idealized data, in reality, both inputs involve varying levels of manual interaction. As an initial study, we conducted tests on the effects of



(a)



(b)

Figure 3. Reconstruction simulation experiment constrained to a two-material system demonstrating the importance of *a priori* information. Knowing the location of the inclusion allowed the algorithm to quickly search the objective function space and arrive (a) back at the original [correct] elasticity contrast (b). Note that the optimization had actually already converged at iteration 7.

degradation in data quality on the end reconstruction. The first experiment used additive image noise to obscure the underlying texture to reflect possible scenarios of corruption during acquisition. Noise fields were created from a zero-mean Gaussian random distribution along the variance of non-background pixels and scaled according to the total power at 1, 5, 10, 15, 20, 25, and 30%. The increasing noise had a confounding impact on the ability of the similarity metric to make a proper match. It was found that the reconstruction was tolerant of image noise up to approximately 10%. Figure 4 demonstrates the degradative effects of image noise.

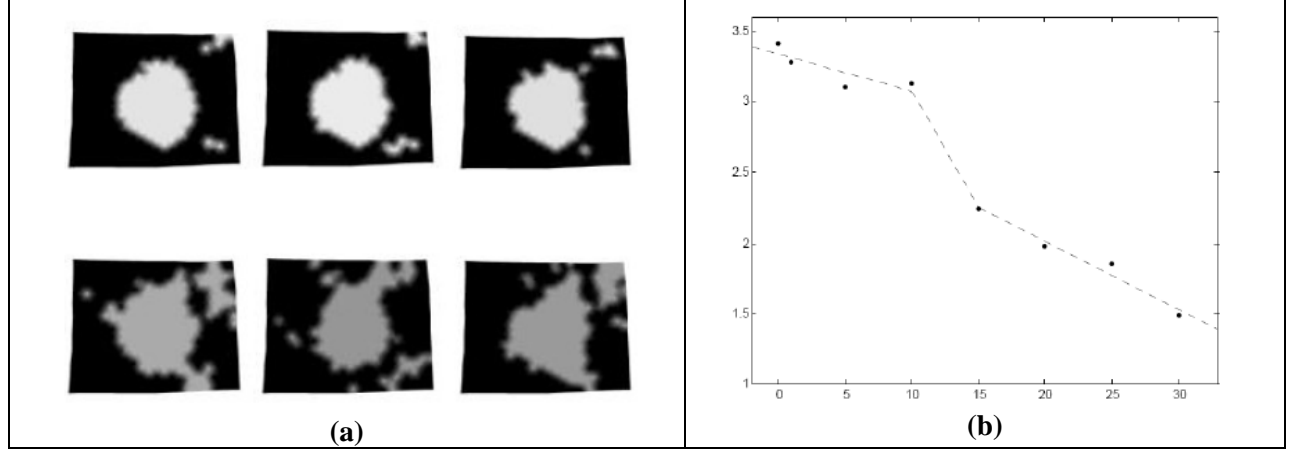


Figure 4. (a) Example 2D reconstructions resulting from the distortion of the target image using additive Gaussian random noise (from top left: 1, 5, 10, 20, 25, 30%). The true elasticity distribution is a centrally located and roughly circular region, and the noise progressively confounds the reconstruction. (b) The decreasing trend of reconstruction fidelity as determined by quantitative evaluation of localizing and characterizing the detected inclusion from a given trial. [see Appendix B]

The second experiment involved boundary condition selection error. Currently, point correspondence at the outer boundary of the domain is determined using a semi-automated fit; a polynomial interpolation is used to make the initial match, and then corrected manually based on salient features. By perturbing the displacements for each boundary node of the finite element mesh, typical user interaction (e.g. visual cues and input device control) can be simulated. A gold standard set of boundary conditions known to produce an accurate reconstruction was modified using randomized vectors of equal magnitude (0.1, 0.2, 0.3, 0.5, 0.75, 1.0, 1.5, and 2.0 pixel units) reflecting a range of typical localization skill for users from poor to expert. It was noted that randomizing all vectors can actually result in twisting of elements that resulted in significant alterations of displacements in the interior of the mesh, leading to grossly inaccurate model deformations. However, boundary condition mismatching of less than 0.5 pixel units was generally tolerated by the reconstruction algorithm, a range that is relatively easily achieved for most users. For further detail, please see the full text of this work as listed in Appendix B.

It should be noted that the ordinate axis in Figure 4(b) is a ‘quality of reconstruction score’ (QRS) that has been developed within the context of this project in order to quantify the localization accuracy of the method. In comparison and conjunction with more standard measure in the elastography field of contrast-to-noise ratio [5], QRS has been used to determine relevant positional and material characterization in both simulation and data studies. The metric is

determined by a classification of the reconstruction [6] that is then compared to the (known) segmentation of the actual elasticity distribution. By examining the rate of accurately selecting an element of the domain to be of the correct material class, a conditional probability closely related to the positive predictive value of the test is obtained; we have determined *a posteriori* that a QRS>80% is typically indicative of a successful reconstruction. The use of QRS can (and will be) similarly applied to the analysis of forthcoming 3D reconstruction experiments. For further discussion, please see material in Appendix A and B.

Proposed work involving the use of a feature tracking and frequency domain analysis is under investigation but not completed at this time. As more data sets are collected, it is hoped that establishing a pattern for understanding the reconstruction algorithm behavior will become statistically relevant.

Specific Aim #3 stated: **“To engineer a device that can accurately produce compressive forces necessary for phantom setups within current clinical imaging systems, providing the basis for a future device that can be used in a clinical setting.”**

A compression device has been constructed and tested in magnetic resonance (MR) and X-ray computed tomography (CT) imaging systems using a polyvinyl alcohol phantom and contrast agents. The compression device is composed of a rectangular Plexiglas frame that traps the phantom in at least two directions with a sliding wall and the compression plate, which houses an air bladder in a polycarbonate frame. When inflated, the air bladder provides a deformation of up to 5 cm. The prototypical phantom used has been fabricated as a polyvinyl alcohol cryogel (~650 cc, 6-8% wt/vol, 1 or 2 free-thaw-cycles) in a manner consistent with the methods presented in [7, 8]. The result is a dome shape approximately 10-11 cm at the base and tapering over a depth of about 5-6 cm. The system has been imaged by both MR and CT scans, with contrast agents of copper sulfate and iodine solution, respectively, having been used to enhance the signals. Volumetric renderings of example scans using minimal post-processing are shown below in Figure 5; note that the device frame is clearly present in the CT image because of its density but is invisible on MR.

A prototype compression chamber that is more clinically oriented has been designed to fit into the chassis of a Philips Intera breast coil unit. It has just recently been fabricated from clear acrylic tube segments in which the air bladders are attached using polycarbonate pins and then covered with an expandable nylon sheet (see Figure 6). Image acquisition studies are currently being designed to utilize this system.

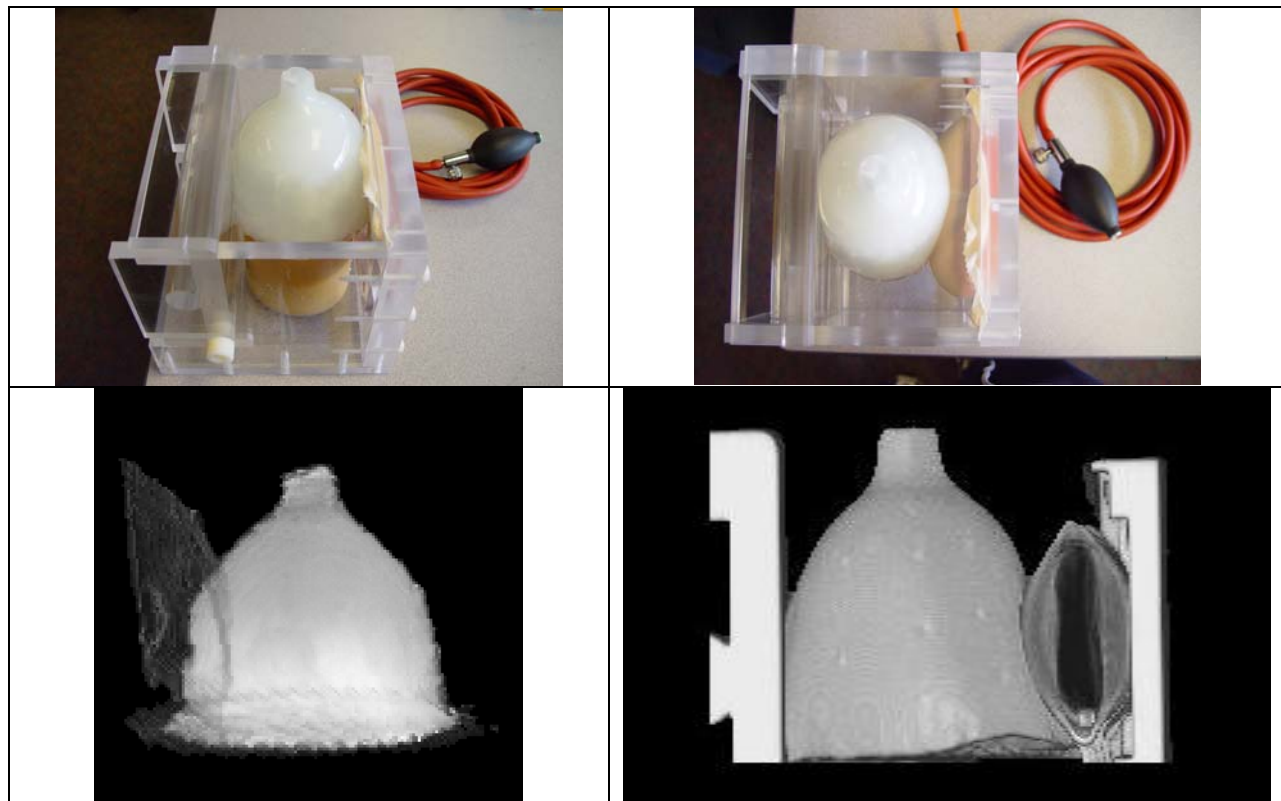


Figure 5. Top row: Photographs of the polyvinyl alcohol phantom inside the compression device without (left) and with compression (right). Bottom row: Surface renderings of from image volumes obtained on a breast phantom in MR (left) and CT (right) scanners while enclosed in the compression device and with the air bladder engaged to provide a deformation.

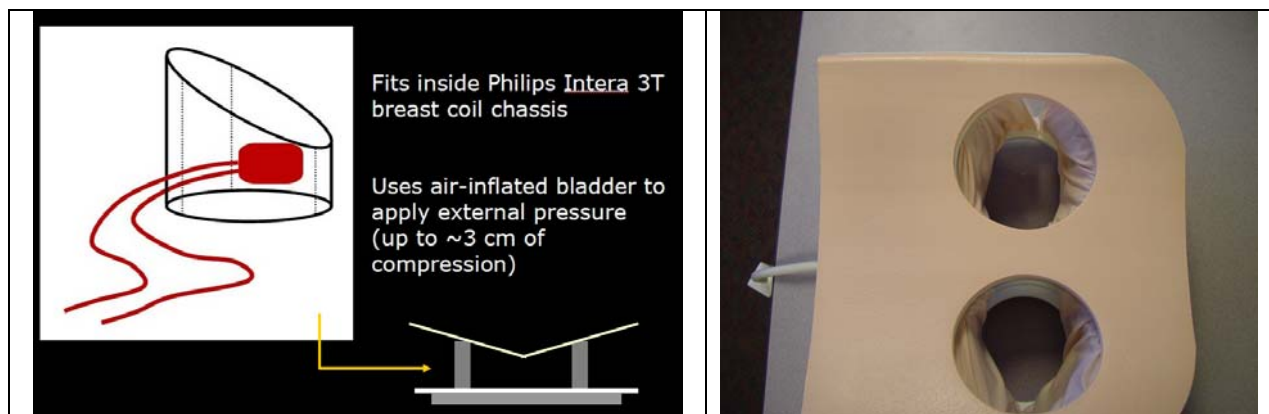


Figure 6. Left: Schematic of compression device designed for clinical use breast coil. Right: Photograph of assembly looking down into the Philips Intera chassis.

Key Research Accomplishments

It has been observed both prior to and during the attempt to extend the MIE technique to cover fully three-dimensional data that the problem is potentially intractable due to the large computational demand and inherently ill-constrained system. The demonstration of a parallelized code base is for this project a significant finding in that it confirms that operating on volumetric images and models is a reasonable working hypothesis, albeit still challenging.

Reportable Outcomes

Work on the MIE method has so far resulted in two conference papers and an additional poster presentation. Prior work that was completed in the reporting timeline resulted in a peer-reviewed journal publication. These items are in part providing the foundation for a thesis proposal to be submitted in the near future. Didactic coursework requirements for the PhD degree have also been completed at this time.

Poster presentations

Vanderbilt University Institute of Imaging Science retreat (June 2005)

Vanderbilt University Medical Scientist Training Program retreat (July 2005)

Conference papers

Ou JJ, Barnes SL, Miga MI, “Application of multi-resolution modality independent elastography for detection of multiple anomalous objects”, *SPIE Medical Imaging 2006*.

Ou JJ, Barnes SL, Miga MI, “Preliminary testing of sensitivity to input data quality in an elastographic reconstruction method”, *IEEE International Symposium on Biomedical Imaging 2006*.

Schuler DR, **Ou JJ**, Barnes SL, Miga MI, “Automatic surface correspondence methods for a deformed breast”, *SPIE Medical Imaging 2006*.

Journal publications

Miga MI, Rothney MP, **Ou JJ**, “Modality independent elastography (MIE): Potential applications in dermoscopy”, *Medical Physics*, vol. 32 (5), pp. 1308-1320, 2005.

Conclusions

The current results and progress denoted in this report are within the proposed statement of work and are encouraging towards completion of the overall objectives with further effort. No significant deviations are reported at this time.

References

- [1] Garra BS, Cespedes I, Ophir J, et al. Elastography of breast lesion:Initial clinical results. *Radiology* 1997;202:79–86.
- [2] McKnight AL, Kugel JL, Rossman PJ, Manduca A, Hartmann LC, Ehman RL. MR Elastography of Breast Cancer: Preliminary Results. (2002) *Am. J. Roentgenol.* 178, 1411-1417
- [3] Balay S, Buschelman K, Eijkhout V, Gropp WD, Kaushik D, Knepley MG, McInnes LC, Smith BF, Zhang H. “PETSc Users Manual”, ANL-95/11 Revision 2.1.5. Argonne National Laboratory, 2004.
- [4] Balay S, Gropp WD, McInnes LC, Smith BF. “Efficient Management of Parallelism in Object Oriented Numerical Software Libraries”, Modern Software Tools in Scientific Computing. Birkhauser Press, pp. 163-202, 1997.
- [5] Doyley MM, Weaver JB, Van Houten EEW, Kennedy FE, Paulsen KD. “Thresholds for detecting and characterizing focal lesions using steady-state MR elastography,” *Medical Physics*, vol. 30(4), pp. 495-504, 2003.
- [6] N. Otsu. “A threshold selection method from gray-level histograms,” *IEEE Trans Syst Man Cybern*, vol. 9, pp. 62-66, 1979.
- [7] Kenneth Chu, Polyvinyl Alcohol Cryogel ; An ideal Phantom Material for MR Studies of arterial flow and Elasticity, Magnetic Resonance in Medicine, Vol 37, pp 314-319, 1989.
- [8] Brusseau E, Fromageau J, Finet G, Delachartre P, Vray D. “Axial strain imaging of intravascular data: results on polyvinyl alcohol cryogel phantoms and carotid artery,” *Ultrasound Med Biol*, vol 27(12), pp. 1631-1642, 2001.

Appendix

The following is a listing of original works referred to in the Body of the Report. Full reprints and other relevant supplemental material are provided after this description.

		Page
A.	Ou JJ, Barnes SL, Miga MI, “Application of multi-resolution modality independent elastography for detection of multiple anomalous objects”, <i>SPIE Medical Imaging 2006</i> . (Condensed) slides from oral presentation, February 2006.	1 10
B.	Ou JJ, Barnes SL, Miga MI, “Preliminary testing of sensitivity to input data quality in an elastographic reconstruction method”, <i>IEEE International Symposium on Biomedical Imaging 2006</i> . (Condensed) slide of poster presentation, April 2006.	19 23
C.	Miga MI, Rothney MP, Ou JJ, “Modality independent elastography (MIE): Potential applications in dermoscopy”, <i>Medical Physics</i> , vol. 32, no. 5, pp. 1308-1320, 2005.	24

Application of multi-resolution modality independent elastography for detection of multiple anomalous objects

Jao J. Ou, Stephanie L. Barnes, Michael I. Miga

{jao.ou,steph.barnes,michael.i.miga}@vanderbilt.edu

Vanderbilt University, Department of Biomedical Engineering, Nashville, TN 37235

ABSTRACT

This work extends a recently realized inverse problem technique of extracting soft tissue elasticity information via non-rigid model-based image registration. The algorithm uses the elastic properties of the tissue in a biomechanical model to achieve maximal similarity between image data acquired under different states of loading. A new multi-resolution, non-linear optimization framework has been employed which allows for improved performance and object detection. Prior studies have demonstrated successful reconstructions from images of a tissue-like thin membrane phantom with a single embedded inclusion that was significantly stiffer than its surroundings. For this investigation, a similar phantom was fabricated with two stiff inclusions to test the effectiveness of this method in discriminating multiple smaller objects. Elasticity values generated from both simulation and real data testing scenarios provided sufficient contrast for detection and good quantitative localization of the inclusion areas.

Keywords: Elastography, elasticity imaging, multi-resolution methods, image similarity, finite elements

1. INTRODUCTION

The practice of palpating soft tissue structures in the course of the clinical physical exam has had a long-standing history of providing correlation of improper stiffness with pathology. The ability to characterize the mechanical properties of tissue is a potential source of additional information relevant for detection and diagnosis of a disease process, and has implications for the assessment of treatment. One way in which this could be achieved in a minimally invasive manner is by analyzing tissue deformation through imaging and/or image processing techniques, which is a central goal of the field of elastography [1]. Application of such methods to the interrogation of the breast [2,3], skin [4-6], prostate [7], and other accessible organ systems is an emerging area of research.

Many of the current elastography methods are founded in ultrasound (US) and magnetic resonance imaging (MR) and involve the estimation of induced displacements within the tissue of interest to infer the elasticity distribution. We have pursued the development of a reconstruction method utilizing quasi-static deformation and image similarity metrics that has been termed 'modality-independent elastography' (MIE) [8-10] because of its potential to handle native anatomical image data from different modalities with simple modification to the acquisition procedure. Common problems facing all of these methods involve limitations with the accurate recovery of elastic property values, detection of small lesions in tissue, and the resolution of multiple discrete lesions [11,12]. Building upon recent study involving a single focal lesion [6], the objectives of this work were to challenge the ability of the MIE method to reconstruct a scenario of two small inclusions embedded in a homogeneous domain and to further explore the feasibility of the method in handling image data from different imaging modalities. This was accomplished by performing simulated reconstructions using images obtained from X-ray computed tomography (CT), MR, and digital photography and then a reconstruction from a real-world experiment using a thin phantom membrane.

2. METHODS

2.1 Elastographic reconstruction framework

The conceptual framework for our elastographic reconstruction has been previously described in [6,8-10]. In brief, an image of a tissue of interest (*source*) is deformed by a biomechanical computer model and compared against an acquired image of the same tissue in a mechanically loaded state (*target*). The deformation and comparison is repeated

using systemic updates of elasticity parameters until a suitable match in intramodal image similarity is achieved in a least squares manner to satisfy a multi-resolution, non-linear optimization scheme. This process can be classified as an inverse problem, with model-based deformation of the source image representing the forward problem. Each of the three major components (model, image comparison, and optimization) is described in more detail in the following sections, and a flow chart representation of the overall process is included in Figure 1.

2.1.1 Biomechanical model

A central component to the model-based inverse problem is the manner in which the continuum is represented. While the constitutive model that best describes tissue deformation mechanics is more complex, for this work, linear isotropic elasticity has been employed. The partial differential equation that expresses a state of mechanical equilibrium can be written as [13]:

$$\nabla \bullet \sigma = 0 \quad (1)$$

where σ is the Cartesian stress tensor.

For the purposes of the following experimentation, we also apply either the plane stress or plane strain approximations to the thin membrane and breast cross-section trials, respectively. The direct consequence of this is a reduction of the 36 stiffness constraints in the general 3D formulation of Cauchy's Law to the two parameters of Young's modulus (E) and Poisson's ratio (ν) in 2D. These simplifications, while significant, are appropriate descriptions of sufficiently thin and thick systems under planar loading. In plane stress,

$$\begin{bmatrix} \sigma_x \\ \sigma_y \\ \tau_{xy} \end{bmatrix} = \frac{E}{(1-\nu^2)} \begin{bmatrix} 1 & \nu & 0 \\ \nu & 1 & 0 \\ 0 & 0 & (1-\nu)/2 \end{bmatrix} \begin{bmatrix} \varepsilon_x \\ \varepsilon_y \\ \gamma_{xy} \end{bmatrix} \quad (2)$$

describes the constitutive relationship between the Cartesian stress tensor $[\sigma_x, \sigma_y, \tau_{xy}]$ and strain tensor $[\varepsilon_x, \varepsilon_y, \gamma_{xy}]$. Similarly, in plane strain,

$$\begin{bmatrix} \sigma_x \\ \sigma_y \\ \tau_{xy} \end{bmatrix} = \frac{E(1-\nu)}{(1+\nu)(1-2\nu)} \begin{bmatrix} 1 & \nu/(1-\nu) & 0 \\ \nu/(1-\nu) & 1 & 0 \\ 0 & 0 & \frac{(1-2\nu)}{2(1-\nu)} \end{bmatrix} \begin{bmatrix} \varepsilon_x \\ \varepsilon_y \\ \gamma_{xy} \end{bmatrix} \quad (3)$$

A finite element (FE) model using triangular elements is constructed from the source image and assigned appropriate boundary conditions based on estimated displacement or stress (i.e. Dirichlet and Neumann conditions, respectively). The standard Galerkin method of weighted residuals [14] is used to construct and solve the system.

2.1.2 Image deformation and comparison

To further describe the reconstruction process, we introduce some additional terminology at this point. The *model domain* is equivalent to the total area of the FE mesh constructed using the *source* image as stated above and contains the relevant elasticity information. The model domain is partitioned by a K-means clustering of the element centroids (MATLAB R14, Mathworks, Natick, MA) into N number of *regions*, each of which has a distinct set of spatially homogeneous elastic properties. Subdividing in this manner allows for the implementation of the multi-resolution reconstruction whereby progressively finer spatial distributions of elasticity parameters are utilized in the process, a method that improves upon previous versions using only a single resolution [8-10]. Analogously, the *comparison domain* is an area specified by semi-automated segmentation on the *target* image and contains information pertaining to image similarity. The comparison domain is separated into M number of rectangular *zones* containing approximately equal numbers of pixels.

The reconstruction algorithm begins by assigning an initial Young's modulus value to each of the regions at the coarsest resolution. Poisson's ratio is held constant at $\nu = 0.485$ to represent a nearly incompressible material. The FE model is solved to determine the nodal mesh displacements, which are in turn used to deform the source image. This model-deformed image is then compared to the target image for every zone using an intensity-based image similarity metric. While a number of methods are available for such a task, here, we utilize the correlation coefficient (CC) [15] throughout, as it has empirically demonstrated superior performance over other metrics such as the sum of squared differences and normalized mutual information.

2.1.3 Optimization scheme

Let \mathbf{T} be a function that represents the model-based image deformation and takes as its input a vector of elastic modulus values \mathbf{E} of length N that corresponds to the current distribution of regions in the model domain. Then for two distributions of modulus values \mathbf{E}_1 and \mathbf{E}_2 , the similarity between the images produced by $\mathbf{T}(\mathbf{E}_1)$ and $\mathbf{T}(\mathbf{E}_2)$ is the vector \mathbf{S} of length M containing evaluations of the correlation coefficient corresponding to the distribution of zones in the comparison domain. The elasticity parameter optimization can be written as the minimization of the least squares error objective function

$$\Psi = |S_{TRUE} - S_{EST}|^2 \quad (4)$$

where \mathbf{S}_{TRUE} is the set of similarity values achieved when comparing the target image to itself, \mathbf{S}_{EST} is the similarity between the model-deformed source and the target images using current estimates of the elastic modulus distribution, and $|\cdot|$ denotes the vector L_2 norm. By definition, \mathbf{S}_{TRUE} is the maximum value for the similarity metric (max CC = 1). Using a Levenberg-Marquardt approach, the residual form of equation (4) becomes

$$[\mathbf{J}^T \mathbf{J} + \alpha \mathbf{I}] \{\Delta \mathbf{E}\} = [\mathbf{J}^T] \{S_{TRUE} - S_{EST}\} \quad (5)$$

where $\mathbf{J} = \partial \mathbf{S}_{EST} / \partial \mathbf{E}$ is the Jacobian matrix of size $M \times N$ and \mathbf{I} is the $N \times N$ identity matrix. Because $\mathbf{J}^T \mathbf{J}$ is typically an ill-conditioned term, the regularization parameter α is determined using the methods described in [16]. Modulus values of the regions at a given resolution are updated by $\Delta \mathbf{E}$ until an error tolerance is reached or a maximum number of iterations have been completed. Upon reaching a stopping criterion, the material property description is interpolated onto the next (i.e. finer) resolution and the above steps are repeated. Spatial averaging of modulus values within the model domain and solution relaxation between successive resolution levels are also utilized to improve the stability of the optimization.

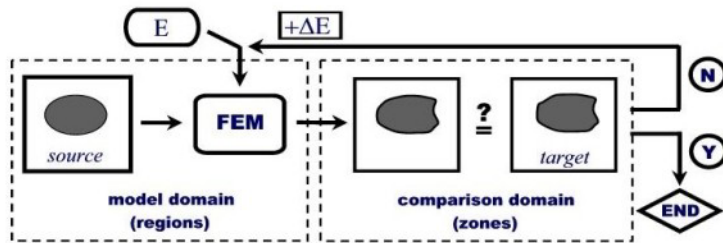


Figure 1. Flow chart of elastographic reconstruction framework.

2.2 Reconstruction experiments

A two-material phantom membrane of simulated skin had been previously constructed [6] using Smooth-On™ polyurethanes (Smooth-On, Easton, PA) designated by the manufacturer as Evergreen 10 and Evergreen 50. These materials have essentially indistinguishable colors but vary significantly in their elastic modulus values, so the former was used as the bulk material and the latter for stiff objects. From material testing, the elastic modulus contrast was expected to be approximately 5.7:1. The phantom was made to contain two circular stiff inclusions 1.5 cm in diameter

embedded near opposing corners of a rectangular field of bulk material measuring 15 cm x 14 cm. A black permanent marker was used to place a pattern of regularly spaced (~1 cm) grid lines across the membrane. The thin membrane was securely clamped along two opposite edges and then subjected to a uniaxial tensile displacement (~8% strain) by means of a milling vise. A commercial webcam (Logitech QuickCam Pro 4000, 960 x 1280 pixel resolution) was rigidly mounted above the membrane to acquire image pairs of the pre- and post-stretched states.

To initially test the method regarding the two-inclusion scenario, a simulation using the source image of the membrane was performed by deforming it with a prescribed model (plane stress) of known boundary displacements and elasticity parameters to generate a target image; high modulus values were assigned to elements bounded by a segmentation of the inclusion locations. A reconstruction was then performed using the actual image data acquired as described above. In both cases, resolutions of $N = 16, 64, 256, 512$, and 800 regions and $M = 400$ zones were used. The results of the idealized and real data reconstructions are shown in Figures 4 and 5, with further quantitative evaluation in Table 1.

In order to examine the robustness of the method regarding its use of data from differing sources, simulation reconstructions were performed using image slices extracted from breast image volumes obtained from CT and MR scans (see Figure 3). Although these were taken from two different patients, the images were selected to be approximately corresponding slices ~2 cm away from the chest wall in the coronal orientation of the standard anatomical position. The simulations were set up in the same manner as for the digital photographs, using either one or two inclusions of about 1 cm in diameter embedded within the true elasticity distribution and a small compression (~8% strain) in the cranial-caudal direction. The relative stiffness of the inclusions was designated to be 5.7:1 for consistency with the material testing data and also because the value is fairly representative of breast tumor properties [17]. The plane strain model approximation was used in the breast simulation trials, progressing through resolutions of $N = 24, 64, 256$, and 576 regions using $M = 200$ zones. The reconstruction method was then run for all four test cases, and the results are presented in Figures 6 and 7 and Table 2.

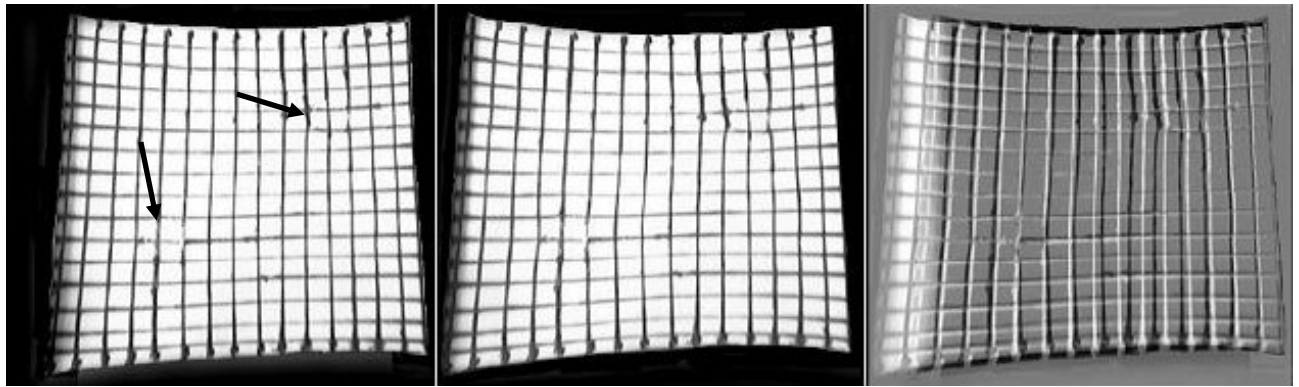


Figure 2. (Left to right): Phantom membrane in undeformed state (*source image*), under deformation (*target image*), and difference image. Arrows in the left panel indicate the positions of the two stiff inclusions.

2.3 Reconstruction evaluation

The fidelity of the elasticity reconstruction was evaluated on its ability to detect the presence of an inclusion based on classification of the material property distribution, and the retrospective accuracy of localizing the lesions. The elastic properties as a whole were treated as a Gaussian mixture of two classes and separated by a threshold established via the method described in [18]. The likelihood of detecting a lesion in the elasticity image was found using the contrast-to-noise ratio as defined by [12,19]:

$$CNR = \sqrt{\frac{2(\mu_L - \mu_B)^2}{\sigma_L^2 + \sigma_B^2}} \quad (6)$$

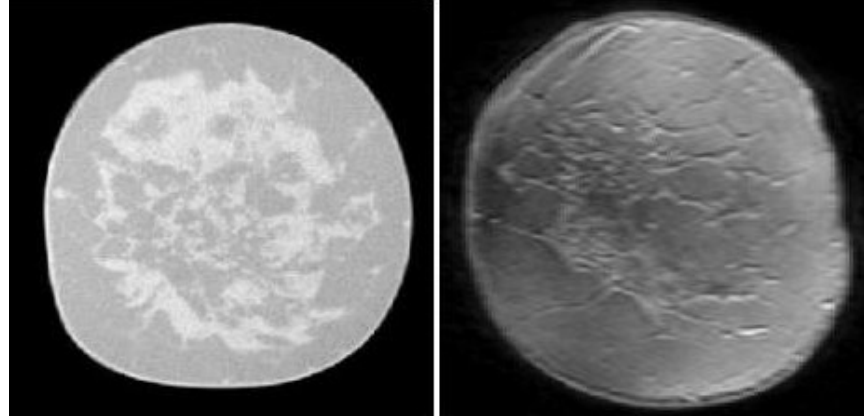


Figure 3. Images slices of breast tissue extracted from a CT volume (left) and MR volume (right) used in simulation study of the ability of the reconstruction method to utilize disparate image data types.

where μ and σ^2 are the sample mean and variance of a material property distribution and the subscripts L and B denote the lesion and bulk material classes, respectively. As a quantitative assessment of the localization of the lesion(s), the positive predictive value of correctly identifying a lesion material within the known segmented region of the inclusions was used as a 'quality of reconstruction score' (QRS). This value is significant because identification of the lesion border and material classification are done independently, so any user knowledge of the test scenario does not influence the performance of the measure. Cutoffs for successful detection and localization were set at $\text{CNR} \geq 2.2$ as noted by [12] and $\text{QRS} \geq 80\%$ as determined by prior study in our laboratory. The average modulus contrast is found from the ratio of the means of the two material classes, and a peak modulus contrast value is also reported by taking the ratio of two manually selected homogeneous regions of approximately equal area known to be representative of the two materials. It should be noted that in other work not presented here, the definition of QRS included a weighting factor provided by the estimated reconstruction modulus contrast, but for the current purposes, only localization accuracy was considered to maintain an objective evaluation of inclusion detection.

3. RESULTS

Figure 4 demonstrates the ability of the reconstruction method to produce an elasticity map from the simulation data with good localization of the inclusions that are easily visually distinguishable from the surrounding bulk material. The progression through resolutions of $N = 64, 256, 512$, and 800 regions shows improving delineation of the inclusions and elastic contrast. Figure 5 demonstrates a similar behavior for the reconstruction of the acquired phantom membrane data, with both spatial definition and modulus contrast increasing with the finer discretization. Table 1 summarizes the quantitative evaluation of the reconstructions in both simulation and phantom trials, including CNR, contrast ratio, and QRS values. The CNR values are sufficient to allow for discrimination of the two materials and the identification of the inclusions was determined to be accurate in both cases. The reconstruction of the phantom membrane does show some misclassification along the border where the deformation was applied as well as in the corner adjacent to one of the inclusions (see Figure 5d).

Figures 6 and 7 show the final reconstruction results for the CT and MR breast slice simulations using either one or two inclusions. In both test scenarios, the resolvability of the stiffer material was found to be adequate according to the CNR threshold, but definitely higher in the MR-derived elasticity images. Localization of the inclusions yielded excellent QRS values in reconstructions using either modality, again higher (though slightly) for the MR images.

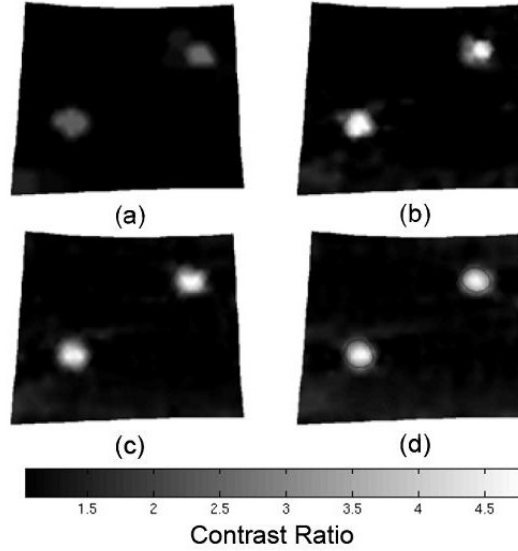


Figure 4. Reconstruction of the simulated membrane deformation using idealized model parameters, progressing through finer resolution distributions (a)-(d) of 64, 256, 512, and 800 regions.

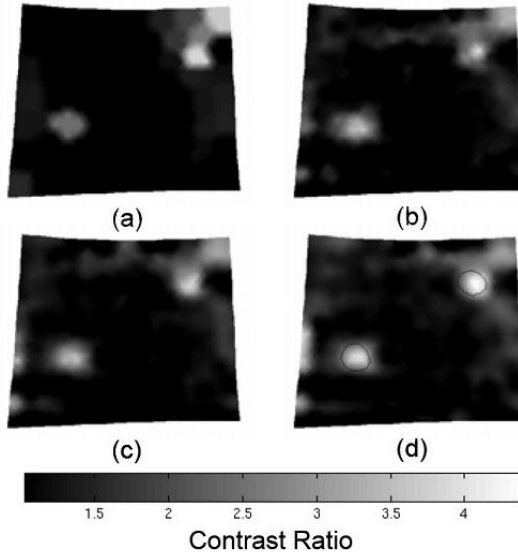


Figure 5. Reconstruction of the actual membrane data. A faint contour in (d) is present to demarcate the actual position of the stiff inclusions. Again, panels (a)-(d) demonstrate the effect of the multi-resolution method in utilizing 64, 256, 512, and 800 regions to better capture the shape and location of the inclusions.

Table 1. Quantitative reconstruction evaluations.

	Avg CR	Max CR	CNR	QRS (%)
Simulation	2.7	4.0	4.4	97.7
Phantom	2.6	4.1	2.8	88.5

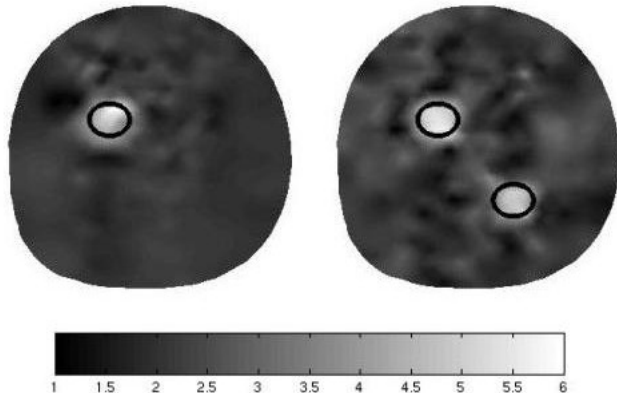


Figure 6. Reconstructions of simulation trials for the CT breast slice using a single inclusion (left) and two inclusions (right). The true inclusion boundaries are overlaid in each elasticity image.

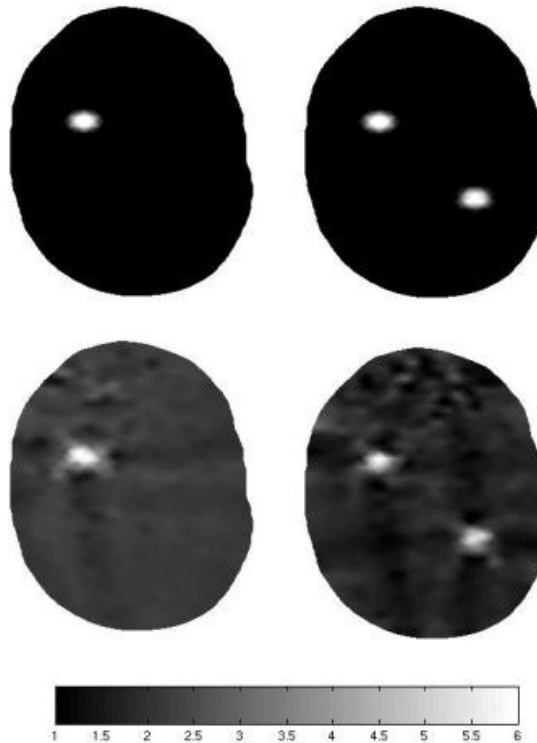


Figure 7. Reconstructions (bottom row) of simulation trials for the MR breast slice using a single inclusion (left) and two inclusions (right). The true elasticity distributions are also shown (top row) for comparison.

Table 2. Quantitative reconstruction evaluations.

	Avg CR	Max CR	CNR	QRS (%)
CT (1 inclusion)	2.1	3.1	3.0	97.6
CT (2 inclusions)	2.0	2.6	3.5	96.9
MR (1 inclusion)	2.8	3.7	20.0	100
MR (2 inclusions)	2.7	3.7	5.7	99.8

4. DISCUSSION

The results of the phantom membrane experiment are encouraging because of their similarity to the idealized simulation. Despite nonlinear model-data mismatch, out-of-plane distortions during stretching, and possible boundary condition inaccuracies, the elasticity reconstruction demonstrated good localization of the two small inclusions. The majority of the problems in reconstruction are mostly likely due to noise incurred in the mapping of the boundary displacements. It should be noted that the phantom reconstruction was achieved with a non-pigmented lesion (see Figure 2, arrows), indicating that deflections of the image structure are capable of driving the image similarity metric of the reconstruction process. This does intuitively suggest that some metric for rating the complexity and density of image pattern in relation to algorithm success may be important and is currently under investigation. Preliminary data not presented in this work indicates that such a threshold does exist for image data that can be properly analyzed by the current framework. The modality independence of the method is also supported by the results here; clearly, the Hounsfield units of CT, floating point values from an MR volume, and the luminance captured by the CCD sensor of a digital camera are quite different types of data to handle because they are based on different physical principles. The simulation reconstructions demonstrate that the method is indifferent to these differences by treating the data as an arbitrary range of intensities and will converge towards the true elasticity distribution based on the image pattern available. This is a possible explanation for the qualitatively more satisfactory results from the MR simulations compared to the CT trials because the distribution of intensities from the former modality yielded a more diversified histogram, an attribute that should naturally aid an intensity-based metric.

While an ideal reconstruction would also be accurate in characterizing a lesion by its modulus contrast, our focus in the study was to test the ability of the method to detect and localize the inclusions. In previous experimentation with reconstructions of single focal lesions, we have been generally successful in achieving a contrast ratio within 25% of the true/expected value. It is somewhat troubling that the contrast ratios calculated here did not meet that criterion, although the experiments with the phantom membrane came fairly close (28%). However, these results underscore the difficulty of the scenarios in not only having to deal with multiple inclusions but quite small ones in both the true physical sense and also the scale of the domain. Any of the given inclusions tested in simulation and with the real data were detected within a homogeneous domain approximately an order of magnitude larger (e.g., 1.5-cm lesions in a 15 cm x 14 cm domain for the phantom). The expectation of being able to identify with any confidence the presence of the inclusion is comparable to the observations made in [12] where the test of finding a single 5-mm lesion within a 4 cm x 5 cm domain proved to be the most problematic. Therefore, the localization of the lesions as determined by the CNR and QRS metrics is deemed to be a success, and further investigation into the nature of the method with respect to the scale of the lesion and domain is warranted.

5. CONCLUSIONS

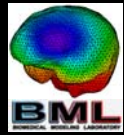
In this work, we have presented further testing of a method for recovering elasticity parameters by maximizing the similarity between images of a tissue of interest acquired under two different states of quasi-static loading within the context of an inverse problem. The specific experiments presented here examined the effectiveness of the technique for the detection of multiple small discrete focal lesions embedded in an otherwise homogeneous medium, as well as further proof-of-concept work in its applicability to utilize image data from various modalities. In both cases, the method provided accurate localization of the lesions based on the reconstruction of relevant elasticity contrast. Because the biomechanical model, multi-resolution optimization, and image acquisition are each modular components of the framework, this elastographic reconstruction technique is readily extensible for added sophistication, and there is ongoing work to enhance the methodology with more complex models and advances in imaging technology.

ACKNOWLEDGMENTS

The authors would like to thank John Boone, PhD of the University of California-Davis, Department of Radiology and Tom Yankeelov, PhD of the Vanderbilt University Institute of Imaging Science for their generous contributions of breast image data (CT and MR, respectively). This work was supported in part by the Whitaker Foundation Young Investigator Award and the Congressionally Directed Medical Research Program BCRP Predoctoral Traineeship Award.

REFERENCES

- [1] J. Ophir, I. Cespedes, H. Ponnekanti, Y. Yazdi, and X. Li, "Elastography - a quantitative method for imaging the elasticity of biological tissues," *Ultrasonic Imaging*, vol. 13, pp. 111-134, 1991.
- [2] A. L. McKnight, J. L. Kugel, P. J. Rossman, A. Manduca, L. C. Hartmann, and R. L. Ehman, "MR elastography of breast cancer: preliminary results," *AJR Am J Roentgenol*, vol. 178(6), pp. 1411-1417, 2002.
- [3] R. Sinkus, M. Tanter, T. Xydeas, S. Catheline, J. Bercoff, M. Fink, "Viscoelastic shear properties of *in vivo* breast lesions measured by MR elastography," *Magn Reson Imaging*, vol. 23(2), pp. 159-165, 2005.
- [4] L. V. Tsap, D. B. Goldgof, S. Sarkar, and P. S. Powers, "A vision-based technique for objective assessment of burn scars," *IEEE Trans Med Imaging*, vol. 17, pp. 620-633, 1998.
- [5] Y. Zhang, D. B. Goldgof, S. Sarkar, and L. V. Tsap, "A modeling approach for burn scar assessment using natural features and elastic property," *IEEE Trans Med Imaging*, vol. 23, pp. 1325-1329, 2004.
- [6] M. I. Miga, M. P. Rothney, and J. J. Ou, "Modality-independent elastography (MIE): potential applications for dermoscopy," *Medical Physics*, vol. 32, pp. 1308-1320, 2005.
- [7] L. Curiel, R. Souchon, O. Rouviere, A. Gelet, and J. Y. Chapelon, "Elastography for the follow-up of high-intensity focused ultrasound prostate cancer treatment: initial comparison with MRI," *Ultrasound Med Biol*, vol. 31(11), pp. 1461-1468, 2005.
- [8] C. W. Washington and M. I. Miga, "Modality independent elastography (MIE): a new approach to elasticity imaging," *IEEE Trans Med Imaging*, vol. 23, pp. 1117-1128, 2004.
- [9] M. I. Miga, "A new approach to elastography using mutual information and finite elements," *Phys Med Biol*, vol. 48, pp. 467-480, 2003.
- [10] M. I. Miga, "A new approach to elastographic imaging: modality independent elastography," *Proceedings of the SPIE*, vol. 4684, pp. 604-611, 2002.
- [11] K. J. Parker, L. S. Taylor, S. Gracewski, and D. J. Rubens, "A unified view of imaging the elastic properties of tissue," *J Acoustical Soc of America*, vol. 117(5), pp. 2705-2712, 2005.
- [12] M. M. Doyley, J. B. Weaver, E. E. W. Van Houten, F. E. Kennedy, and K. D. Paulsen, "Thresholds for detecting and characterizing focal lesions using steady-state MR elastography," *Medical Physics*, vol. 30(4), pp 495-504, 2003.
- [13] A. Boresi, *Elasticity in Engineering Mechanics*, Wiley-Interscience, 2000.
- [14] L. Lapidus and G. F. Pinder, *Numerical Solution of Partial Differential Equations in Science and Engineering*, John Wiley & Sons, 1982.
- [15] J. M. Fitzpatrick, D. L. G. Hill, C. R. Maurer, "Image registration," *Handbook of Medical Imaging*, vol. 2. SPIE Press, pp. 447-513, 2000.
- [16] N. Joachimowicz, C. Pichot, and J. P. Hugonin, "Inverse scattering: an iterative numerical method for electromagnetic imaging. *IEEE Trans Biomed Engineering*, vol. 39, pp. 1742-1752, 1991.
- [17] T. A. Krouskop, T. M. Wheeler, F. Kallel, B. S. Garra, and T. Hall, "Elastic moduli of breast and prostate tissues under compression," *Ultrasonic Imaging*, vol. 20, pp. 260-274, 1998.
- [18] N. Otsu, "A threshold selection method from gray-level histograms," *IEEE Trans Syst Man Cybern*, vol. 9, pp. 62-66, 1979.
- [19] M. Bilgen, "Target detectability in acoustic elastography," *IEEE Trans Ultrason Ferroelectr Freq Control*, vol. 46, pp. 1128-1133, 1997.



13 Feb 2005

Application of Multi-resolution Modality Independent Elastography for Detection of Multiple Anomalous Objects

Jao J. Ou, Stephanie L. Barnes, Michael I. Miga

Vanderbilt University
Dept. of Biomedical Engineering
Nashville, TN 37235



Modality Independent Elastography (MIE) Concepts

- (Solid) tumors are usually stiffer than surrounding tissue
- Soft tissue interrogation of various organ systems (e.g. skin, liver, prostate, breast) for tumor detection
- Elastography gives representation of a structure according to its mechanical properties
- Deformation processes indicative of material inhomogeneity can be captured by imaging and approximated with modeling
- Associate form and function through image analysis separate from modality acquisition



MIE Components

- (1) Biomechanical FE model of soft-tissue deformation
 - Conservation of stresses (continuum)
$$\nabla \bullet \sigma = 0$$
 - Constitutive stress-strain relation (Hooke's Law)
$$\sigma = E\varepsilon$$

MIE Components (cont.)

- (2) Similarity measure for comparing images
 - Acquired "pre-" (source) & "post-" (target) quasi-static deformation
 - Intensity-based registration metrics
 - MI, NMI, SSD, CC, GC

MIE Components (cont.)

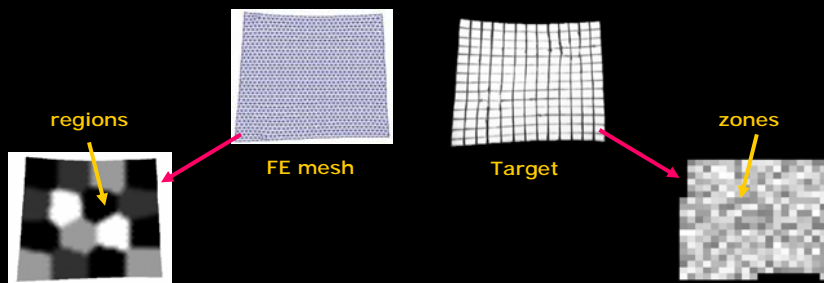
- (3a) Optimization routine to update material properties in the model
- Objective function based on similarity

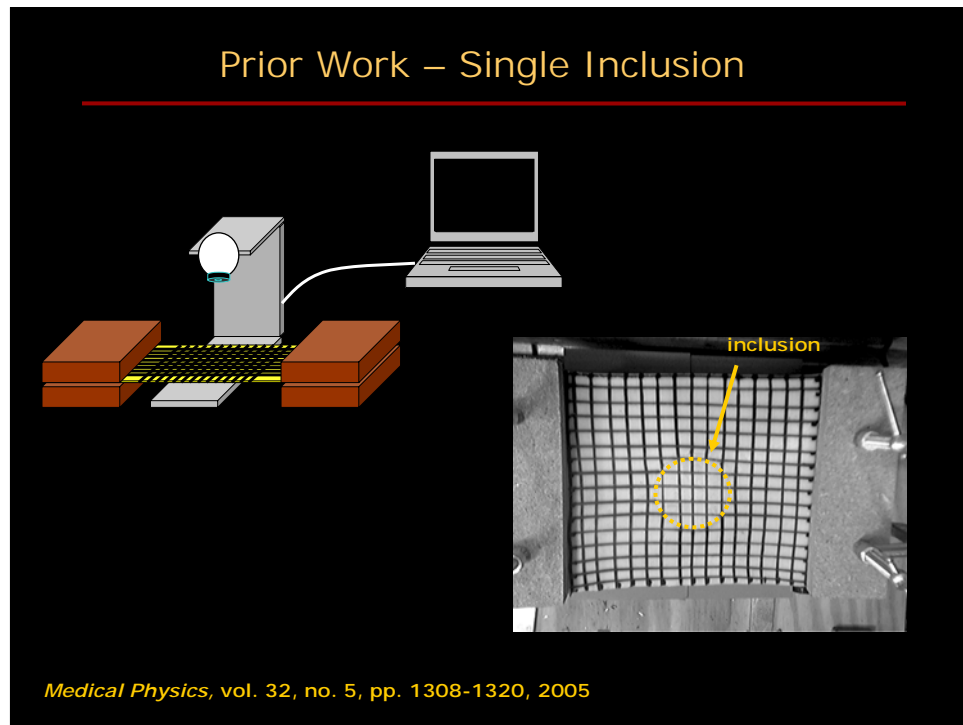
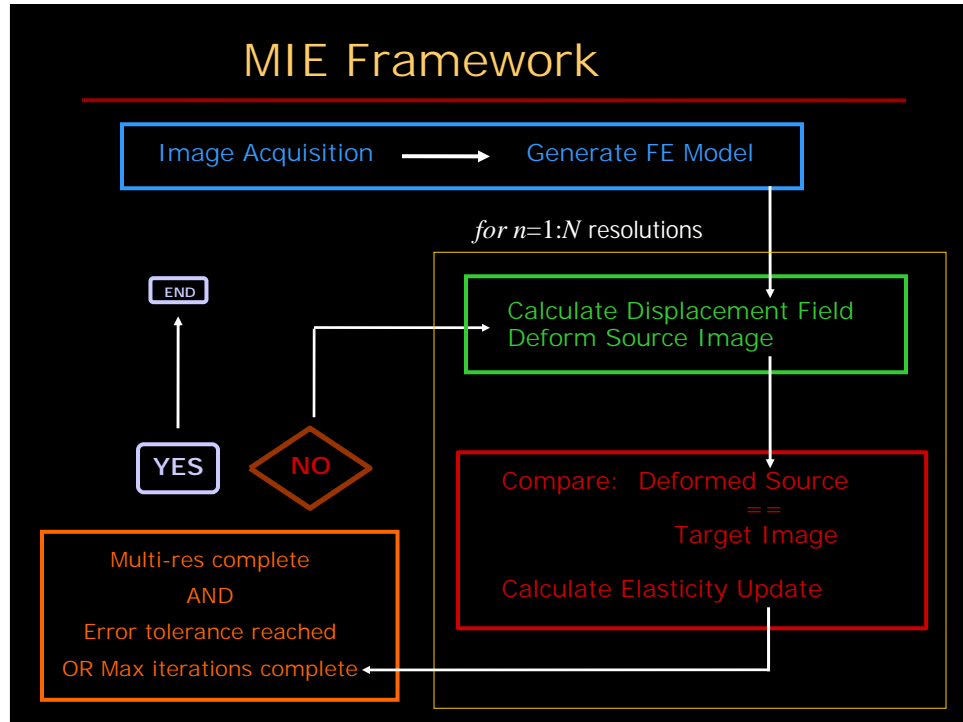
$$\Phi(E) = \sum_{m=1}^M (S(E_T)_m - S(E_E)_m)^2$$
- Levenberg-Marquardt

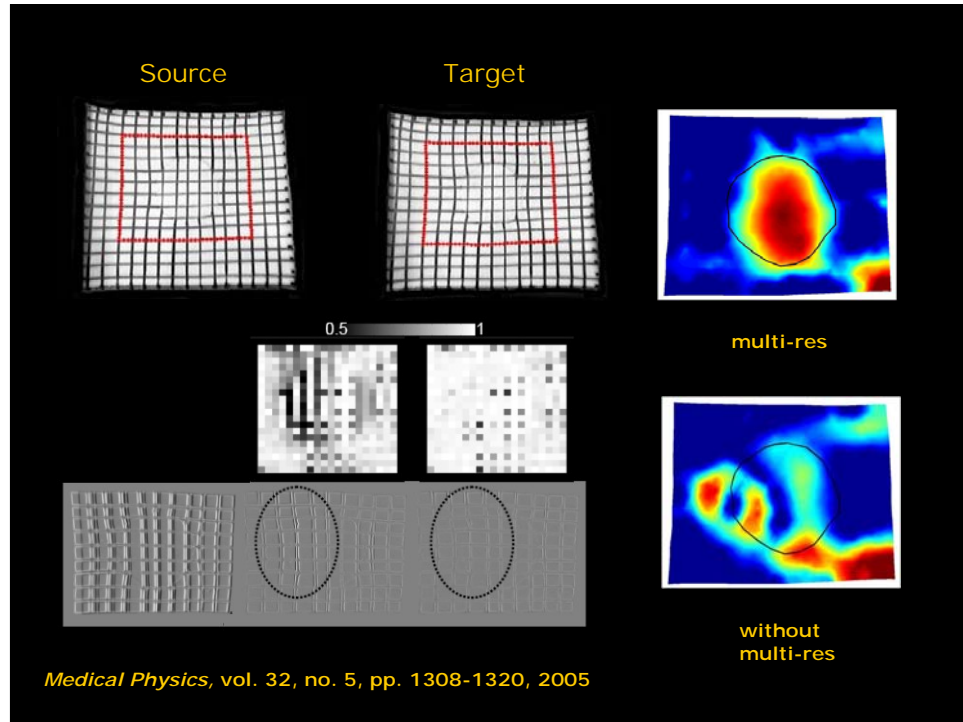
$$(J^T J + \alpha I) \Delta E = J^T (S(E_T) - S(E_E))$$

MIE Components (cont.)

- (3b) Discretization of elasticity distribution and image data
 - Multi-resolution K-means clustering of elements ("regions")
 - Sampling of image comparison area ("zones")







Study Objectives: Further Testing of MIE

- Modality independence
 - Digital photography
 - X-ray computed tomography (CT)
 - Magnetic resonance (MR)
- Two (small) inclusions
- Simulation and phantom membrane study

Evaluating MIE

- Classify reconstruction
Two-class Gaussian mixture model
- Detectability via elasticity image contrast

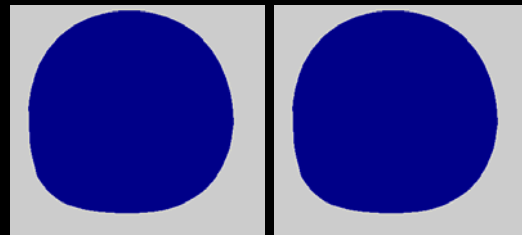
$$CNR = \sqrt{\frac{2(\mu_L - \mu_B)^2}{\sigma_L^2 + \sigma_B^2}} \geq 2.2$$

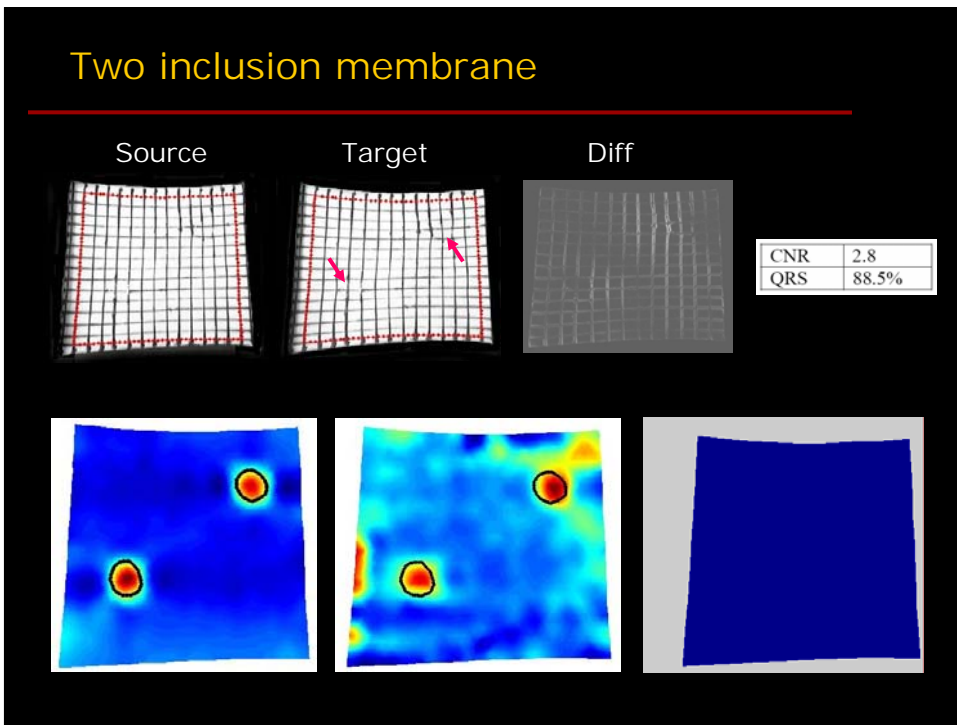
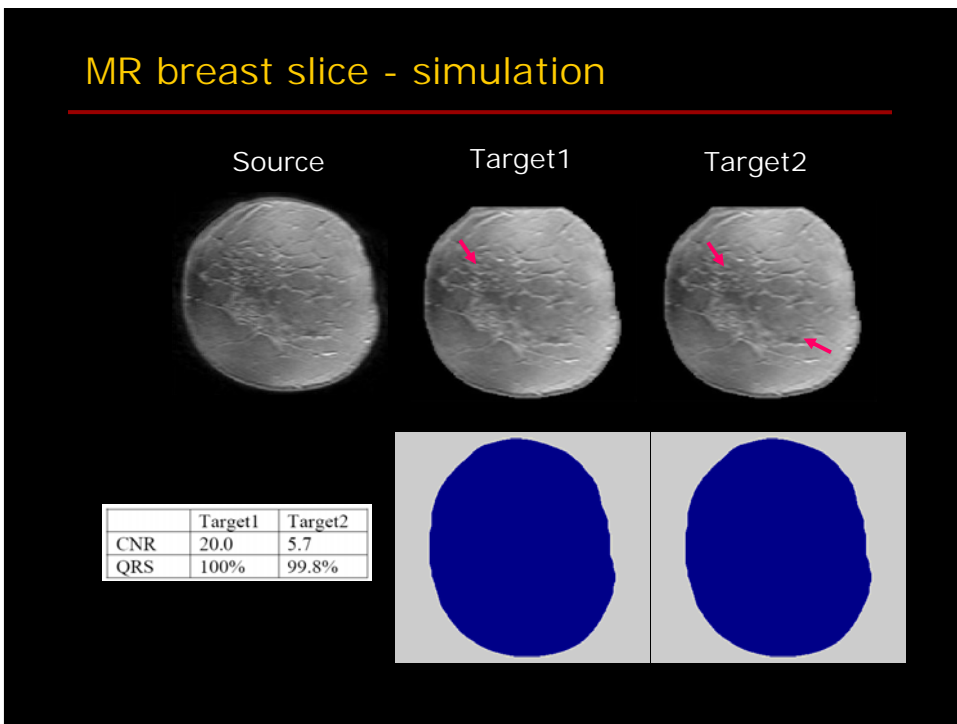
- Localization accuracy
Positive predictive value of identifying lesion material in correct location

$$QRS = \frac{TP}{TP + FP} \geq 80\%$$

CT breast slice - simulation

	Source	Target1	Target2





Summary

- Modality independence via simulation for handling various data types
- Multi-resolution approach potentially improves optimization convergence
- Two small stiff inclusions reconstructed in phantom membrane experiment
- Detectability accomplished via CNR
- Localization successful as evaluated by QRS

Acknowledgments

- BML/SNARL
Richard Chen
Prashanth Dimpuri
- John Boone, PhD (CT data)
- Tom Yankeelov, PhD (MR data)
- Whitaker Foundation
- CDMRP/BCRP Pre-doctoral Fellowship



<finis>

Future Directions / Research Questions

- Biological tissues are not typically linearly elastic
- Need for accurate boundary conditions creates dependence on segmentation methodology
- Not all data sets necessarily contain sufficient information for elastographic reconstruction

PRELIMINARY TESTING OF SENSITIVITY TO INPUT DATA QUALITY IN AN ELASTOGRAPHIC RECONSTRUCTION METHOD

Jao J. Ou, Stephanie L. Barnes, Michael I. Miga

Vanderbilt University, Department of Biomedical Engineering, Nashville, TN 37235
 {jao.ou,steph.barnes,michael.i.miga}@vanderbilt.edu

ABSTRACT

An elastographic reconstruction method has been developed to recover the material properties of soft tissue by model-based analysis of image data acquired at different states of mechanical loading. The algorithm utilizes image similarity as part of the cost function for a multi-resolution, non-linear optimization. Previous work with a phantom membrane used for simulated dermoscopic application has prompted this preliminary investigation of the relative effects of additive image noise and boundary condition determination errors on the performance of the method. The results as quantified by elasticity contrast and localization accuracy indicate that the reconstruction process is robust in the presence of realistic levels of image corruption and tolerates the majority of boundary condition mapping errors.

1. INTRODUCTION

The practice of palpating soft tissue structures in the course of the physical exam for assessing tissue health has had a long-standing clinical history of providing correlation between improper stiffness and pathology. The ability to characterize the mechanical properties of tissue is therefore a potential source of information relevant for both diagnosis and prognosis. One way in which this could be achieved in a non-invasive manner is through analysis of tissue deformation with imaging and image processing techniques, which is a central goal of the field of elastography [1].

The conceptual framework for our elastographic reconstruction has been previously described in [2-4]. In brief, images of a tissue of interest are acquired in an initial (*source*) and then mechanically loaded state (*target*). The source image is deformed by a prescribed computational model and compared to the target. This is repeated in an iterative process using updates to the elasticity parameters of the model as generated by a multi-resolution, non-linear optimization scheme in order to achieve a suitable match in image similarity. Because the goal of the reconstruction is to

determine a spatial mapping of tissue elasticity, this process can also be classified as an inverse problem.

Our observations during the ongoing development and testing of this method have prompted questions concerning the quality of data necessary and sufficient to achieve satisfactory results (i.e. fidelity of the reconstructed elasticity image). The primary inputs to the reconstruction method are the acquired images and the delineated boundary conditions on the region of interest. While it is clearly preferable to have idealized data, in reality, both inputs involve varying levels of manual interaction. As an initial study, we have sought to test the effects of degradation in data quality on the end reconstruction by using additive image noise and randomized boundary condition selection error.

2. METHODS

2.1. Elastographic Reconstruction Framework

There are three major components in the reconstruction framework: a biomechanical model of tissue response to applied deformation, a method of image comparison, and an optimization scheme. For the current version, a continuum-based model of mechanical equilibrium using isotropic Hookean linear elasticity with a plane stress approximation is employed [5]. This allows for a reduction of the general 3D formulation of Cauchy's Law to the two parameters of Young's modulus and Poisson's ratio in 2D. The displacement solution of the finite element representation of the model, solved using the standard Galerkin method of weighted residuals [6], is then applied to the nodes of a simple triangular mesh based on the source image domain in order to perform image deformation. The mesh is partitioned by K-means clustering (MATLAB R14, Mathworks, Natick, MA) into N number of *regions*, each of which describes a distinct set of homogeneous elastic properties for a grouping of adjacent elements. This allows for implementation of the multi-resolution approach by creating a hierarchy of increasingly finer spatial distributions of elasticity parameters, which has been shown to be an improvement upon previous versions using only a

single resolution [2,3]. A second discretization is performed to divide the target image into M number of rectangular *zones* containing approximately equal numbers of pixels. The deformed source image is compared to the target using an intensity-based image similarity metric (here, the correlation coefficient [7]) in the evaluation of the least squares error objective function

$$\sum_{m=1}^M (S_{TRUE} - S_{EST})^2 \quad (1)$$

where S_{TRUE} is an $M \times 1$ vector of the (maximum) similarity values achieved when comparing the target image to itself and S_{EST} is the $M \times 1$ vector of similarity between the target and model-deformed source image created using current estimates of the elastic modulus distribution. It should be noted that S_{TRUE} has by definition a value of 1 for the correlation coefficient.

The minimization of equation (1) using a Levenberg-Marquardt approach takes the form

$$[J^T J + \alpha I] \{\Delta E\} = [J^T \{S_{TRUE} - S_{EST}\}] \quad (2)$$

where J is the Jacobian matrix of size $M \times N$ estimating $\partial S / \partial E$, ΔE is the $N \times 1$ vectors of updates to the current elasticity values, and α is the scalar regularization term for the Hessian matrix as described in [8].

2.2. Material Preparation and Image Acquisition

For our simulation purposes, a two-material skin phantom had been previously constructed [2] as a thin membrane measuring 15 cm x 15 cm, with a single 5-cm circular stiff inclusion embedded in the center (Figure 1). The phantom was manufactured with Smooth-On™ polyurethanes (Smooth-On, Easton, PA) Evergreen 10 and Evergreen 50. These materials have essentially indistinguishable colors but vary significantly in their elastic modulus values, so the former was used as the bulk material and the latter for the inclusion. Based on material testing, the expected contrast ratio of Young's modulus values was determined to be approximately 5.7:1. A black permanent marker was used to place a pattern of regularly spaced (~ 1 cm) grid lines on the membrane. The membrane was clamped along two opposite edges and then stretched in a uniaxial fashion by means of a milling vise. A commercial webcam (Logitech QuickCam Pro 4000) was mounted above the assembly to acquire image pairs of the membrane in pre- and post-stretched states (960 x 1280 pixel resolution, 8-bit grayscale).

2.3. Reconstruction Experiments

Based on prior work, a data set consisting of a particular image pair and associated boundary conditions

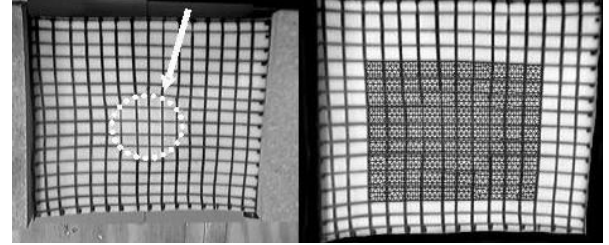


Figure 1. Experimental phantom membrane system (left) and input image with overlaid finite element mesh (right). The inclusion location is indicated by the arrow and dotted line. The mesh designates the actual region reconstructed.

known to produce a satisfactory reconstruction was designated as the gold standard for the remainder of the experiments (Figure 1). In order to test the effect of increasing amounts of additive noise on the reconstruction algorithm, Gaussian random fields of 1, 5, 10, 15, 20, 25, and 30% noise were applied to the base target image in three separate trials. This presents a challenge that ascertains the ability of the similarity metric and objective function to discern a proper match.

The current method for selecting Dirichlet boundary conditions on the finite element mesh is semi-automated and requires the user to make a final determination on point correspondence. The second experiment was intended to simulate the targeting error of the user (e.g. visual cues and input device control). Each test involved applying randomized vectors of equal magnitude to alter the boundary conditions of the gold standard data set. Errors of 0.1, 0.2, 0.3, 0.5, 0.75, 1.0, 1.5, and 2.0 mesh units (scaled to be equivalent to pixel coordinates) were used in two separate trials for a total of 16 reconstructions. Sub-pixel magnitudes were included after determining that the accuracy of selecting a feature point in the image/mesh was typically less than or equal to 0.5 units for users ranging from moderate to expert skill.

For all reconstructions, resolutions progressing through $N = 16, 36, 64, 144, 256$, and 400 regions and $M = 9$ similarity zones were used; domains were initialized to homogeneous elasticity and Poisson's ratio held constant at 0.485 to represent nearly incompressible material(s).

2.4. Reconstruction Analysis

The final reconstructed elasticity values were modeled as a mixture of two Gaussian distributions, and a threshold was established to maximize inter-class variation [9] and subsequently classify each region as bulk or stiff material. Because Dirichlet boundary conditions are exclusively used in these reconstructions, the method is only sensitive to relative differences in elasticity. The quantities used in evaluating reconstruction success are the elasticity contrast ratio, localization accuracy of the inclusion, and an overall measure designated the 'quality of reconstruction score' (QRS). The elasticity contrast ratio (CR) was calculated

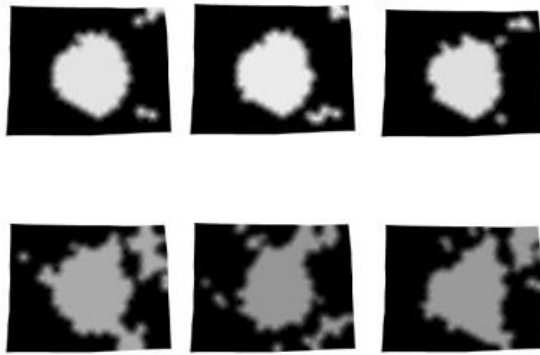


Figure 2. Representative reconstructions with image noise. From top left: 1, 5, 10, 20, 25, and 30% additive Gaussian noise. The reconstructions are visualized as two materials, with whiter areas indicating higher elasticity contrast values.

Table 1. Reconstruction quality under noise conditions

Additive image noise							
% Noise	1	5	10	15	20	25	30
LA	0.92	0.90	0.91	0.70	0.69	0.66	0.56
CR	3.56	3.45	3.45	3.24	2.88	2.83	2.68

Gold standard: LA = 0.95, CR = 3.60

Boundary condition error								
Err	0.1	0.2	0.3	0.5	0.75	1.0	1.5	
AE	0.96	3.32	2.21	102	0.93	32.2	12.6	7.66
LA	0.87	0.92	0.88	0.59	0.94	0.86	0.86	0.96
CR	3.63	3.68	3.44	2.91	3.46	3.71	3.78	3.30

CR = elasticity contrast ratio, LA = localization accuracy
AE = initial alignment error (%), Err = error magnitude.

from the mean values of the two material classes, and the positive predictive value of identifying stiff material within the independently segmented boundary of the inclusion gives a measure of localization accuracy (LA). The quality of reconstruction is simply then the product $QRS = CR * LA$, which allows the user to consider the other two measures in conjunction.

3. RESULTS

Figures 2 and 3 show examples of reconstructions achieved under various image noise and boundary condition errors, and individual localization errors and contrast ratio values are listed in Table 1. Note that the data for the image noise experiment was averaged from the three trials, and that the data presented for the boundary condition experiment is from one [representative] trial. Figure 4 is a plot of the reconstruction quality decreasing with increasing image noise, and Figure 5 shows the reconstruction quality trend plotted against the change in initial alignment error (detailed in the following section) relative to that of the gold standard.

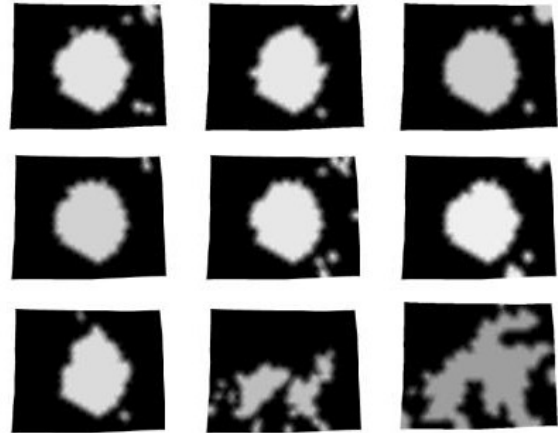


Figure 3. Representative reconstructions with boundary condition error. Left to right: 0.1, 0.2, 0.3 units (top row); 0.75, 1.0, 2.0 units (middle row, trial #1); 0.75, 1.0, 2.0 units (bottom row, trial #2). Error magnitudes greater than or equal to 0.5 mesh units are not accurate predictors of reconstruction quality.

4. DISCUSSION

From visual inspection of Figure 2, it is apparent that the achieved reconstruction becomes more inaccurate with increased image noise. However, the ability to identify and localize the stiff inclusion is not significantly impaired until a noise field of greater than 10% is applied. The threshold was found by determining which level of noise provided the best minimum sum squared error fit of two lines to the distribution of reconstruction quality in Figure 4. This would indicate that the similarity metric and objective function are robust to intensity deviations of about 6 gray levels. While Gaussian noise is one of several possible types and may not always be an ideal model, it is still relevant to acquisition inaccuracy and corruption processes that may be encountered across several medical imaging modalities. The use of an intensity-based similarity metric appears to give the method an advantage in being generally insensitive to reasonably expected amounts of image noise.

Figure 3 demonstrates that because of the random nature of the boundary condition errors, the magnitude is itself not an accurate indicator of reconstruction quality. This necessitated the introduction of a more suitable parameter that accounts for the net effect of the altered boundary conditions in order to perform fair evaluations. In essence, randomizing the vectors at every node causes the optimization to use an unpredictable starting pose and increases its chance of converging to an improper minimum. Therefore, the ‘initial alignment error’ (AE) is defined as the relative percent change between the objective function evaluation using the gold standard boundary conditions and those of the test case. An as example, it could be assumed that vectors of magnitude 0.5 would be a much more tolerable error than 2.0, but it is the significantly larger AE

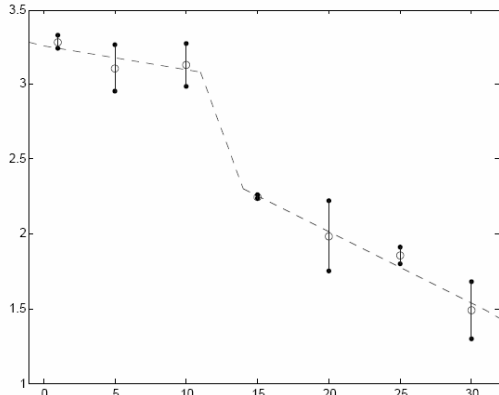


Figure 4. Reconstruction quality vs. percent additive image noise. The drop-off after 10% additive noise indicates the threshold of tolerance for the method.

of the former that actually predicts the poor outcome. However, it should also be noted (results not shown here) that even if the same set of error vectors are scaled over varying magnitudes, there is no clear trend in alignment error or reconstruction quality. This appears to imply that certain boundary nodes, most likely those in the direction of largest strain, have a greater effect on reconstruction and merit particular care in selection. Other factors influencing unfavorable reconstructions are most likely nonlinear effects not predicted by the current model as well as an inherent lack of discrimination by intensity-based similarity metrics in analyzing the regularity of the imposed grid pattern. Nevertheless, for the error magnitudes tested that best approximate realistic inaccuracies (i.e. <0.5 units), the alignment errors were small and quality of the end reconstruction was seen to be quite good. This qualitatively validates the current method of determining point correspondence as a reasonable procedure with an accommodating margin (factor of four) in light of typical user interaction.

5. CONCLUSIONS

In this work, we have presented a method for recovering elasticity parameters from image data of thin membrane structures by maximizing the image similarity between two different states of mechanical loading within the context of an inverse problem. The biomechanical model, multi-resolution optimization, and image acquisition are each modular components of this elastographic reconstruction framework, making it extensible to added sophistication. Tests were conducted to examine the tolerance of the method to degraded or improper inputs. The results indicate that the gold standard data set was mostly optimal for obtaining a successful reconstruction. Widening disparities in either image data or boundary condition selection from that in the gold standard caused observable trends of declining reconstruction quality. Based on these observations, it appears that the method handles most

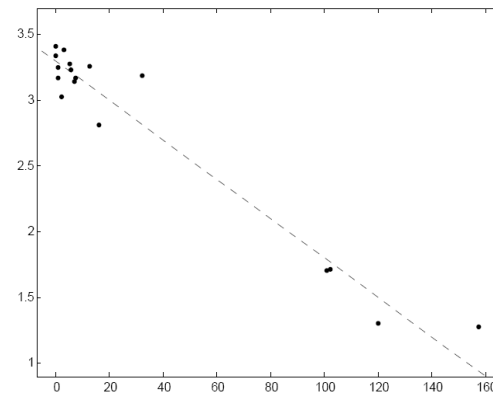


Figure 5. Reconstruction quality vs. percent change in initial alignment relative to gold standard. The majority of errors tested produced satisfactory reconstructions.

expected variations encountered in image acquisition as well as the majority of typical user inaccuracies. Because there are complicated effects associated with mapping of the Dirichlet boundary conditions in constraining the displacement solution of the model, further study on inter-rater variability in selection as well as comparisons with more automated point correspondence methods is ongoing.

Acknowledgements This work was supported in part by a Whitaker Foundation Young Investigator Continuation Award and the Congressionally Directed Medical Research Program – Breast Cancer Research Program Pre-doctoral Fellowship.

6. REFERENCES

- [1] J. Ophir, I. Cespedes, H. Ponnekanti, Y. Yazdi, and X. Li, "Elastography - a quantitative method for imaging the elasticity of biological tissues," *Ultrasonic Imaging*, vol 13, pp. 111-134, 1991.
- [2] M.I. Miga, M.P. Rothney, J.J. Ou, "Modality-independent elastography (MIE): potential applications for dermoscopy," *Medical Physics*, vol 32 pp. 1308-1320, 2005.
- [3] C.W. Washington, M.I. Miga, "Modality independent elastography (MIE): a new approach to elasticity imaging," *IEEE Trans Med Imaging*, vol 23, pp. 1117-1128, 2004.
- [4] M.I. Miga, "A new approach to elastography using mutual information and finite elements," *Phys Med Biol*, vol 48, pp. 467-480, 2003.
- [5] Boresi, A., *Elasticity in Engineering Mechanics*, Wiley-Interscience, 2000.
- [6] Lapidus, L., and G.F. Pinder, *Numerical Solution of Partial Differential Equations in Science and Engineering*, John Wiley & Sons, 1982.
- [7] Fitzpatrick, J.M., Hill, D.L.G., and C.R. Maurer, "Image registration," *Handbook of Medical Imaging, Volume 2*. SPIE Press, pp. 447-513, 2000.
- [8] N. Joachimowicz, C. Pichot, J.P. Hugonin, "Inverse scattering: an iterative numerical method for electromagnetic imaging," *IEEE Trans Biomed Engineering*, vol 39, pp. 1742-1752, 1991.
- [9] N. Otsu, "A threshold selection method from gray-level histograms," *IEEE Trans Syst Man Cybern*, vol 9, pp. 62-66, 1979.



PRELIMINARY TESTING OF SENSITIVITY TO INPUT DATA QUALITY IN AN ELASTOGRAPHIC RECONSTRUCTION METHOD



Jao J. Ou, Stephanie L. Barnes, and Michael I. Miga
Vanderbilt University, Department of Biomedical Engineering, Nashville, TN 37235

BACKGROUND

Changes to the local cytoarchitecture induced in a variety of pathologies can manifest as alterations in tissue mechanics that are relatively easy to evaluate. Many elastography methods are typically dependent on the specific modality and for which they were developed (e.g. magnetic resonance and ultrasound imaging). We have developed modality-independent elastography (MIE) as a reconstruction method that recovers the material properties of soft tissue via model-based analysis of image data acquired at different states of mechanical loading. The algorithm utilizes image similarity in the performance of a multi-resolution, non-linear optimization. Previous work with a phantom membrane and for simulated dermoscopy applications prompted this work as an investigation of the effect of additive noise corruption and boundary condition determination errors on the performance of the method. The results as quantified by elasticity contrast and localization accuracy indicate that the reconstruction process is robust in the presence of realistic levels of image corruption and tolerates the majority of boundary condition mapping errors.

PURPOSE

The inputs to the reconstruction process are in two major forms: image data and boundary condition estimation. Inadequate fidelity in either quantity is capable of affecting the success of the reconstruction through some form of model-data mismatch. We proposed to test the sensitivity of the algorithm to various levels of an applied noise process by altering either the intensity distribution of the target image or the displacement vectors defining the Dirichlet boundary conditions.

METHODS

Figure 1. Flow chart of MIE. After acquisition, source and target images (A) are discretized into regions and zones, respectively. The reconstruction process involves updating elastic modulus values (B,E) to drive a finite element model-based image deformation (C) until the best match is found (D).

RESULTS

Figure 3. MIE image noise reconstruction experiment.

Gaussian random fields of variable strength with respect to the variance of non-background pixel values were applied in an additive fashion to the target image. Shown in the left column from top to bottom are the original target and three with 10%, 20%, and 30% noise. The middle column shows the corresponding elasticity reconstructions after application of a thresholding scheme to classify bulk (black) and inclusion materials (white/gray). The right column shows the pixel prediction value of identifying the correct material type within the proper boundaries as well as the mean elasticity contrast of the overall distribution. For this work, our overall evaluation of reconstruction quality is expressed as the product of these two quantities. The effect of additive noise is to decrease reconstruction quality as evidenced in the progressively poorer localization of the inclusion.

Figure 4. MIE boundary condition noise reconstruction experiment.

Randomized vectors of a particular magnitude were applied to the boundary condition specifications of the same finite element mesh used for all reconstructions. This simulates targeting error by the user in the currently semi-automated method of point correspondence selection, and the effect is illustrated in the top row from left to right, the gold standard boundary and then with m-estimation of 0.75, 1.0, and 2.0 mesh units (equivalent to pixel coordinates) in the Dirichlet conditions (slightly exaggerated scale for visual effect). The corresponding reconstructions in the middle and bottom rows demonstrate that two different trials using the same magnitude of randomized vectors can effect very different levels of reconstruction quality.

Figure 5. Reconstruction quality vs. image noise.

Three trials of image noise were performed (shown averaged and with standard error bars); the drop-off in reconstruction quality indicates the presence of a threshold at approximately 10% additive Gaussian noise.

Figure 6. Reconstruction quality vs. boundary condition noise.

Two trials of eight levels of noise ranging from 0.1 to 2.0 mesh units were performed. Each reconstruction was treated as a separate data point based on its initial alignment error, defined here as the relative change between the objective function evaluation using the gold standard boundary conditions and those of the [randomized] test case.

DISCUSSION

Figures 3 and 5 show that the achieved reconstruction becomes more inaccurate with increased image noise. However, the ability to identify and localize the stiff inclusion is not significantly impaired until a noise field of greater than 10% is applied. The threshold was found by determining which level of noise provided the best minimum sum squared error fit of two lines to the distribution of reconstruction quality. This would indicate that the similarity metric and objective function are robust to intensity deviations of about 6 gray levels in a 8-bit image. While Gaussian noise may not always be an ideal model, as a preliminary point of investigation, it is still relevant to acquisition inaccuracy and corruption processes that can be encountered across several medical imaging modalities.

Figure 4 demonstrates that the magnitude of the random vectors is itself not an accurate indicator of reconstruction quality because the multiple degrees of freedom afforded by the boundary nodes cause the optimization to fall into an unpredictable starting pose, increasing the chance of local minima. The magnitude of the random vectors is also not a good indicator of the alignment error (AE) to provide a consistent means of comparison between trials (Figure 6). As a further example, it could be assumed that vectors of magnitude 0.5 would be a much more tolerable error than 2.0, but it is the significantly larger AE that actually predicts the poor outcome. It should also be noted (results not shown here) that even if the same set of error vectors are scaled over varying magnitudes, there is no clear trend in alignment error or reconstruction quality. This appears to imply that certain boundary nodes, most likely those in the direction of largest strain, have a greater effect on reconstruction and merit particular care in selection. Nevertheless, for the error magnitudes that approximate inaccuracy in boundary condition demarcation (i.e. <0.5 units), the quality of those reconstructions was satisfactory. This qualitatively validates the current method of determining point correspondence as a reasonable procedure with an accommodating margin (factor of four) in light of typical user interaction. Further research is ongoing into validation and control of boundary conditions, as well as more automated methods of point correspondence.

REFERENCES

- M.I. Miga, M.P. Rothery, J.J. Ou, "Modality-independent elastography (MIE): potential applications for dermoscopy," *Medical Physics*, vol 32 pp. 1308-1320, 2005.
- M.I. Miga, "A new approach to elastography using mutual information and finite elements," *Phys Med Biol*, vol 48, pp. 467-480, 2003.
- N. Joachimowicz, C. Pichot, J.P. Hugonin, "Inverse scattering: an iterative numerical method for electromagnetic imaging," *IEEE Trans Biomed Engineering*, vol 39, pp. 1742-1752, 1991.
- N. Otsu, "A threshold selection method from gray-level histograms," *IEEE Trans Syst Man Cybern*, vol 9, pp. 62-66, 1979.

This work was supported in part by a Whitaker Foundation Young Investigator Award and a Congressionally Directed Medical Research Program Breast Cancer Research Program Pre-doctoral Fellowship.

Modality independent elastography (MIE): Potential applications in dermoscopy

Michael I. Miga,^{a)} Megan P. Rothney, and Jao J. Ou

Vanderbilt University, Department of Biomedical Engineering, Nashville, Tennessee 37235

(Received 7 September 2004; revised 7 February 2005; accepted for publication 25 February 2005; published 18 April 2005)

The use of palpation information for skin disease characterization is not as commonly used as in other soft tissues, although mechanical differences within lesions have been noted. For example, regions of hyperkeratosis have the potential to transform into cancerous lesions and likely feature different material properties from those of surrounding normal tissue due to varying cytoarchitecture. As a result, the spatial distribution of lesion mechanical properties may serve to assist a diagnosis or enhance visualization of the complete extent of a cancerous region, i.e., accurate information regarding the margins of disease for surgical therapy. In this work, a multiresolution extension to a novel elastographic imaging method called Modality Independent Elastography (MIE) is used to characterize the mechanical properties of a skin-like phantom embedded with a mock stiff lesion. Simulation studies were also performed to investigate the potential for characterizing realistic melanoma lesions. Elasticity image reconstructions from the phantom experiments localized the stiff inclusion and had good correlation between the Young's modulus contrast ratio and experimental measurements from material testing. In addition, multiresolution MIE was shown to be a more robust framework than its single-resolution version. Results from the melanoma simulation demonstrate the potential for using multiresolution MIE with dermoscopic images. © 2005 American Association of Physicists in Medicine. [DOI: 10.1118/1.1895795]

I. INTRODUCTION

Skin cancers are a growing health concern in the United States, with total annual cases being reported in the millions by the American Cancer Society. There are three major types of skin cancers [basal cell carcinoma (BCC), squamous cell carcinoma (SCC), and melanoma], with melanoma estimated to be the sixth most prevalent cancer and an estimated 55,100 new cases (within the United States) to be diagnosed in 2004.¹ In general, skin cancers develop from precancerous lesions of the epidermis that have dysplastic changes due to the damage inflicted by ultraviolet solar radiation. As with other cancers, the dysfunctional cells may aggressively compete with normal tissue for nutrients and space. The progression from a benign to malignant state depends upon the degree of cellular differentiation and the spatial extent of the growth, which approximately translates into the pathological determination of grade and stage.

When skin cancers are identified at an early stage and are still small in size, surgical excision is usually straightforward and effective. If the disease has progressed to invade deeper levels of the skin, treatment becomes more difficult and may involve more invasive surgery, radiation, and/or chemotherapy. It is clear that the early detection of cancer is critical in order to formulate a proper treatment plan and achieve the most favorable clinical outcome. However, detection and diagnosis still rely primarily on visual inspection followed by a biopsy of suspect areas for histological analysis. Therefore, a significant proportion of diagnostic technological advances have been concerned with obtaining a better view of the lesion via improved optics (i.e., dermoscopy) or more advanced and novel imaging systems ranging from high-

frequency ultrasound to confocal laser microscopy.^{2,3} Additional strategies involving electrical impedance mismatch,⁴ Raman spectroscopy,⁵ and cytological smears³ have also been forthcoming.

As opposed to other methods mentioned above which capitalize on electrical, optical, and biochemical phenomena, we have chosen to pursue an alternative approach to skin health assessment which is based on its mechanical behavior. Detecting changes in tissue by palpation and then associating them with a disease state has had a longstanding history in clinical medicine. Although a health assessment of skin from palpation is performed to a lesser degree, utilizing changes in the mechanical properties to characterize the skin does have precedent within clinical dermatology. One thoughtful review by Edwards and Marks discusses the complex mechanical behavior of skin when subjected to *in vitro* and *in vivo* testing.⁶ Their review highlights extensive methodologies being used to quantify skin mechanical properties (e.g., uniaxial and biaxial extensometry, torsion stimulators, indentometry, ballistometric tests, shear wave application devices, dynamic suction methods, ultrasonics, and electrodynamometry) and also indicates the difficulties in comparing across these methods. As a result, Edwards and Marks emphasize the necessity for quantitative, reproducible methods to assess skin health given the wide subjectivity in clinical analysis.⁶ For example, the work by Draaijers *et al.* suggests that reliable subjective assessment of the pliability of scars requires more than one observer while measurements using a noninvasive suction device can be accomplished with a single observer.⁷ This type of work qualitatively confirms the Edwards and Marks conclusion that the need for technology

and automation in skin assessment will be essential for reducing inter-rater variability.

While the characterization of skin cancer for diagnostic purposes and possibly surgical intervention is an interesting prospect, other investigations have begun to suggest relationships between skin elasticity parameters and other diseases. In a recent study using a noninvasive suction device, Pierard *et al.* demonstrated a correlation between bone mass density (BMD) and skin elasticity parameters. Specifically, in a 100-woman study in which a portion of the subjects were participating in hormone replacement therapy, a positive correlation existed between BMD of the hip and femoral neck and skin elasticity parameters. The authors clearly state that their goal was not to develop a surrogate BMD assessment test, but the results are nevertheless intriguing.^{8,9} Using a similar device, Yoon *et al.* demonstrated a relationship between skin elasticity parameters and patients afflicted with diabetes mellitus.¹⁰ Other work has been forthcoming^{11–16} that demonstrates the potential for using noninvasive measurements of skin mechanical parameters as diagnostic information.

To this end, the field of elastography has established methods to spatially characterize the mechanical properties of tissues under various states of deformation with the goal of developing functional parameters to characterize disease.^{17,18} In skin cancer, increases in cell density, atypia in the morphology and orientation of cells, and compositional alterations (e.g., hyperkeratosis) contribute to changes in the local cytoarchitecture. These changes in mechanical structure can propagate from microscopic to macroscopic levels and may manifest as a distortion of the normal anatomy. Given the influence of mechanical structure on the behavior of deforming tissue, elastographic imaging methods may be well suited for detecting and monitoring the growth of these cancerous anomalies. In fact, advances in applying ultrasound elastography and sonography techniques to skin are being reported.^{3,19–22} Most recently, Gennisson *et al.* demonstrated the use of a new sonoelastographic probe that measured a distinct difference between dermis and hypodermis shear wave velocities which was subsequently used to estimate Young's modulus.²² Although interesting, this work is not completely applicable to the clinical goals of understanding the spatial extents of a melanoma lesion.

Following previous work in Ref. 23, we are using a new elastographic method we have termed "modality-independent elastography" (MIE) that combines nonrigid image registration with an elasticity inverse problem. More specifically, image similarity metrics routinely used with image registration methods are recast within a nonlinear optimization algorithm whereby mechanical properties (e.g., Young's modulus) within a biomechanical model of the deforming tissue become the driving parameters for improved image registration. In this way, the MIE method circumvents two potential limitations of current elastographic techniques. First, it is not inherently dependent on preprocessing steps such as homologous feature selection and tracking which drive active contour models^{19–21} or other traditional displacement-based iterative methods^{24–29} (however, it does require the determination of boundary conditions). Second,

because it is an image processing technique, MIE is not reliant on a particular imaging modality such as in ultrasound and magnetic resonance elastography, as long as the acquired images provide a sufficient pattern to allow for registration. Building on recently completed work with a dual-mesh implementation,³⁰ in this paper we present a simplified multiresolution elasticity imaging framework for Young's modulus reconstruction. In addition, phantom and simulation experiments demonstrate its utility as a dermoscopic image analysis tool for evaluating skin lesions based on material elasticity.

As a final point, the work presented here represents a potentially new application of the MIE approach for the characterization of skin lesions using optical images. This may have significant implications at many length scales (subcellular, cellular, matrix level, and gross tissue). For example, properly designed, optically based MIE could be used to characterize the structural development of tissues at the cellular scale. This could be important for therapies such as Mohs micrographic surgery. Mohs is a surgical technique which combines surgery and pathological investigation to more effectively remove skin tumors. More specifically, after removing visibly cancerous regions, the surgeon removes an additional thin layer of the site margin and creates a "map" of the border. Upon pathological examination of the removed layer, the "map" can be used to target the remaining cancerous cells. Currently, the Mohs technique is a time-consuming procedure, but the success of the procedure is compelling and has been shown to be cost effective with certain considerations.³⁹ If MIE skin imaging could accurately assist or replace the pathologic characterization of the margin in less time, this would be of great value for this surgical therapy.

II. METHODS

A. Model of phantom/skin elasticity

One critical component within all model-based inverse problem frameworks is the selection of a computational model to represent the continuum of interest. In our phantom and simulation studies, we have elected to employ a linear elastic model to simulate the skin. These assumptions (e.g., symmetry, isotropy, etc.) allow the simplification of Cauchy's law from 36 stiffness constants to 2 and employ the equation

$$\nabla \cdot \sigma = 0, \quad (1)$$

where σ is the two-dimensional (2-D) Cartesian stress tensor and is defined as

$$\sigma = \begin{bmatrix} \sigma_x & \tau_{xy} \\ \tau_{xy} & \sigma_y \end{bmatrix}. \quad (2)$$

The constitutive relationships for the material can be written as

$$\begin{bmatrix} \sigma_x \\ \sigma_y \\ \tau \end{bmatrix} = \frac{E}{(1-\nu)^2} \begin{bmatrix} 1 & \nu & 0 \\ \nu & 1 & 0 \\ 0 & 0 & \frac{1-\nu}{2} \end{bmatrix} \begin{bmatrix} \frac{\partial u}{\partial x} \\ \frac{\partial v}{\partial y} \\ \frac{\partial u}{\partial y} + \frac{\partial v}{\partial x} \end{bmatrix}, \quad (3)$$

where E is the Young's modulus, ν is Poisson's ratio, and u , v are displacements in the x and y directions, respectively. For this work, Poisson's ratio was assumed to be constant at 0.485 for our skin phantoms and tissue simulations. This value was found by searching the reconstruction parameter space for an optimal value that achieved maximum similarity when comparing the homogeneous model-deformed image to its acquired counterpart. The constitutive relationships expressed in (3) represent a two-dimensional approximation to a three-dimensional system which assumes a symmetric, isotropic, thin specimen in equilibrium and stresses that are constrained to lie within the plane, i.e. the classic plane stress approximation.³¹ Using the Galerkin method of weighted residuals to integrate this set of partial differential equations, a finite element framework is generated and can be solved to represent a displacement field for a given distribution of Young's modulus values.³² The boundary conditions for our studies below were either manually derived from a structured grid representation as in the phantom system or prescribed by the user in the case of the simulation studies.

B. Modality-independent elastography (MIE)

The MIE framework begins with the acquisition of a baseline predeformed "source" image and a post-deformed "target" image. The "source" image set is used to create a well-resolved finite element mesh of the tissue domain. In previous work, a second coarse mesh was also specified on the domain and was used specifically as the mechanical property reconstruction grid.³⁰ In this work, a new single-mesh region-based multiresolution MIE approach has been employed which simplifies previous dual-grid techniques with the generation of a structured regionalization using a K -means clustering algorithm based on the element centroids of the well-resolved mesh. A K -means clustering algorithm iteratively partitions the element centroids into a given number (K) of *regions* (where K is the user-defined number of desired clusters) such that the sum of all point-to-*region* centroid distances over all *regions* is minimized. The advantage of using the K -means clustering approach as opposed to a regular grid is that the clustering approach can more appropriately fit irregular domains (e.g. the circular domain for the dermoscopic image set). For this work, the implementation in the MATLAB (MathWorks, Natick, MA—www.mathworks.com) statistics toolbox was used. Figure 1 illustrates an example of this approach on a circular domain whereby the element centroids have been clustered into 16 separate homogeneous, isotropic *regions*.

The method has been adapted to a multiresolution strategy whereby coarser resolutions (i.e., fewer *regions*) can be ini-

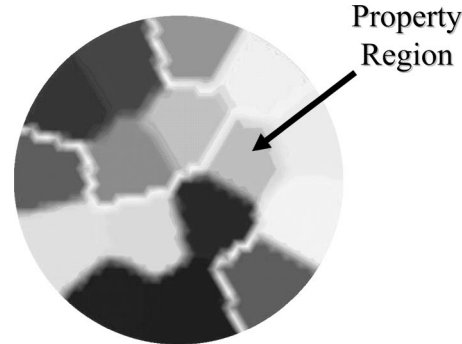


FIG. 1. K -means material property clustering for a circular domain with 16 property regions designated.

tionally reconstructed to provide better initial guesses to subsequent resolutions. The use of hierarchical multiresolution structures within both rigid and nonrigid registration algorithms has a longstanding precedent and lends credence to its application here.^{33–35} In this work, six progressively finer resolutions were used within each reconstruction (16, 36, 64, 144, 256, 400 *regions*).

Once the mesh and K -means resolutions have been specified, the reconstruction algorithm begins by assigning an initial modulus value to each *region* (a homogeneous initialization is assumed) at the first resolution, weighted residual equations are integrated, boundary conditions are applied, and the matrix equation system is generated:

$$[A(\vec{E}_E)]\{u\} = \{b\}, \quad (4)$$

where $[A(\vec{E}_E)]$ represents the model stiffness matrix based on the current distribution of properties \vec{E}_E , $\{u\}$ is the vector of unknown tissue displacements, and $\{b\}$ is the vector of known forces acting on the system and boundary conditions. Upon the calculation of tissue displacements, the source image can be deformed. This model-deformed source image is then compared to the target image using an image similarity method^{23,30} which is calculated over a number of discrete spatial *zones* (e.g., for all reconstructions, approximately 400 similarity *zones* were designated within the image for a comparison). Modulus values in the *regions* are updated based on maximizing the similarity between the deformed source image and the target image over all the similarity *zones* until a tolerance is reached or the desired number of iterations has been completed.

With respect to the optimization framework for MIE, it can be represented as a least squared error objective function:

$$\phi(\vec{E}) = \min\{\|S(\vec{E}_t) - S(\vec{E}_E)\|^2\}, \quad (5)$$

where $S(\vec{E}_t)$ is the similarity value achieved when comparing the target image to itself (i.e., the maximum value for the similarity metric) and $S(\vec{E}_E)$ is the similarity between the model-deformed source image and the target image using the current estimate of the elastic modulus, \vec{E}_E . Equation (5) can be solved by employing a Newton–Raphson-based approach:

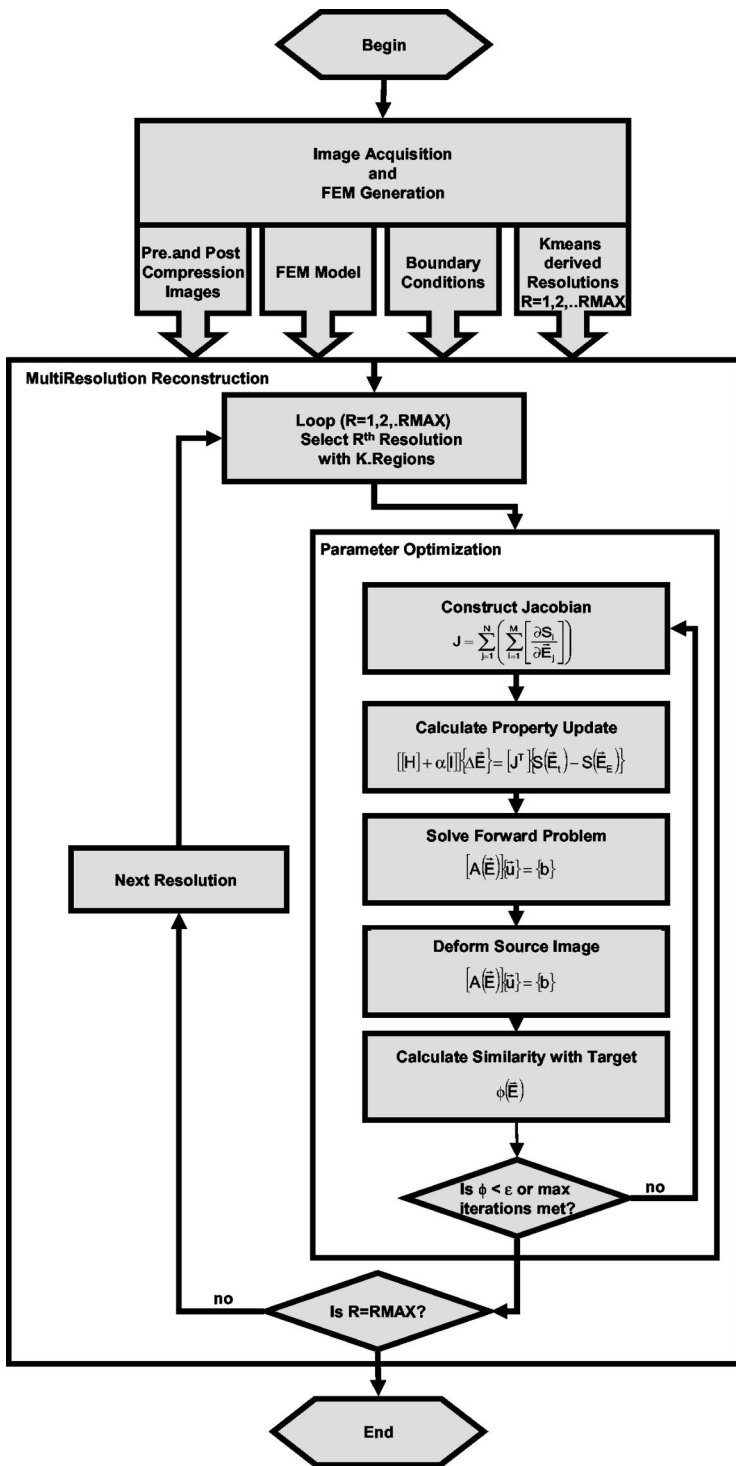


FIG. 2. Multiresolution MIE algorithm flow chart where “ $R=1,2,3,\dots,R_{\text{MAX}}$ ” is the resolution level with R_{MAX} the most well resolved; and “ K ” is the number of material *regions* within a particular resolution “ R ”.

$$[[J^T][J] + \alpha[I]]\{\vec{\Delta E}\} = [J^T]\{S(\vec{E}_t) - S(\vec{E}_E)\}, \quad (6)$$

where $[J]$ is the $M \times N$ Jacobian matrix of the form $J = \partial S(\vec{E}_E) / \partial \vec{E}$, M is the number of similarity measurement *zones*, and N is the number of material property *regions* and is equivalent to K as designated in the K -means clustering algorithm. The details of Eq. (6) have been reported previously.^{23,30} Because $[J^T][J]$ (an approximation to the Hessian matrix) tends to be ill conditioned, it is regularized

with an empirically determined α parameter found in the standard Levenberg–Marquardt approach.³⁶ The determination of this regularization parameter is described in Ref. 37. Figure 2 is a flow chart of the new multiresolution MIE approach.

In previous work, we have analyzed the performance of our MIE algorithm with respect to four standard image similarity metrics found within the literature: the sum of squared differences, normalized mutual information, the correlation

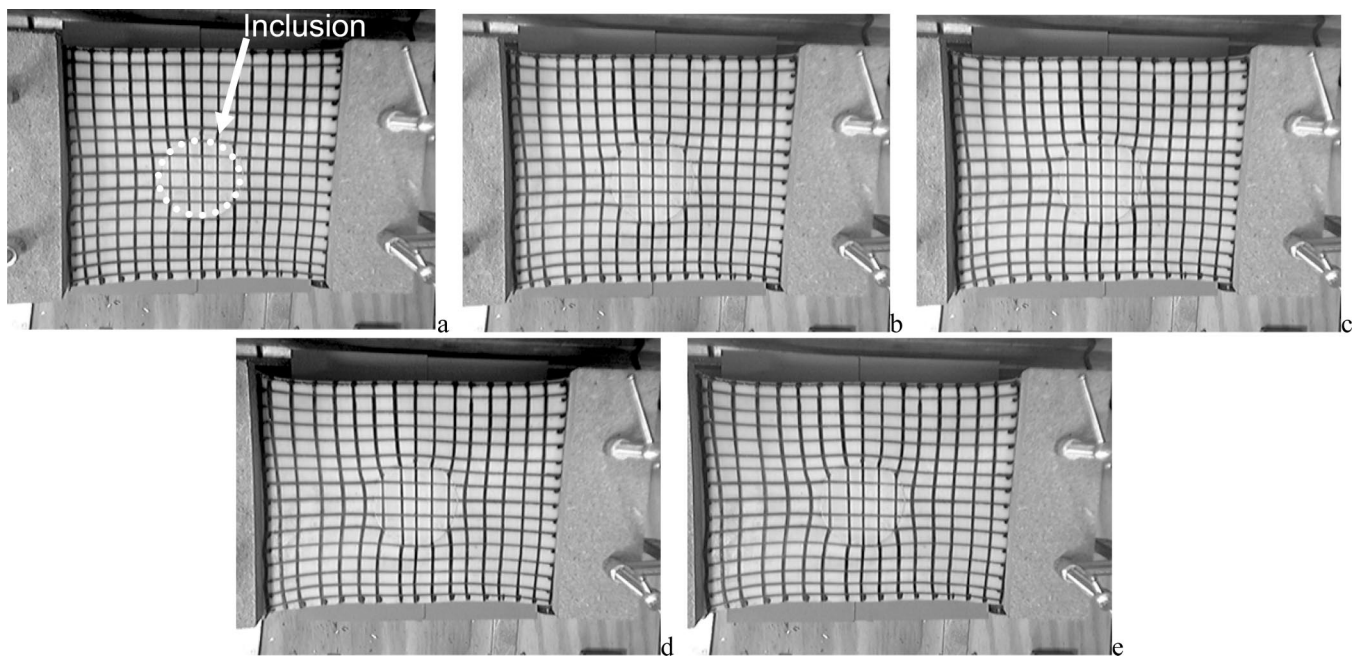


FIG. 3. Experimental data from the skin-stretching setup shown in Fig. 4: (a) baseline, (b) 5 mm, (c) 10 mm, (d) 15 mm, (e) 20 mm.

coefficient (CC), and the gradient correlation coefficient (GC).³⁰ Within this work, the correlation coefficient and gradient correlation coefficient were used for the similarity measurements.

Briefly stated, the CC operates on the distribution and mean intensity values of the overlapping regions of two images where I_1 would represent the intensity values within the “target” image and I_2 would be the model-deformed “source” image. The correlation coefficient can be calculated by the expression

$$CC = \frac{\sum_i (I_1(i) - \bar{I}_1)(I_2(i) - \bar{I}_2)}{\sqrt{\sum_i (I_1(i) - \bar{I}_1)^2 (I_2(i) - \bar{I}_2)^2}}, \quad \forall i \in I_1 \cap I_2, \quad (7)$$

where \bar{I}_1 , \bar{I}_2 are the mean intensity values within each respective image, and i is the i th pixel within the respective image. The GC metric is calculated by applying the correlation coefficient to images that have been processed by any of the standard edge detection functions (e.g., Canny, Sobel, etc.).

C. Phantom construction

A phantom was constructed that was approximately 25 cm long, 15 cm wide, and approximately 2 mm thick. The inclusion-surrounding bulk material of the phantom was Smooth-On™ Evergreen 10 polyurethane with an additive to allow permanent marker to adhere to the material surface (Smooth-On, 2000 Saint John Street, Easton, PA). A cylindrical inclusion was placed centrally within the membrane phantom that was approximately 5 cm in diameter and was made of a stiffer polyurethane material (Smooth-On™ Evergreen 50). The inclusion material was chosen for its relative stiffness to that of Evergreen 10 and its color which is the same (to study the case of non-pigmented lesions). After the phantoms had set, a permanent marker was used to draw

15 cm x 15 cm grid with 1 cm x 1 cm squares on the phantom surface. Figure 3(a) shows the skin phantom used for data collection in this series of experiments.

D. Image acquisition protocol

To acquire the pre- and post-deformed images of the stretched skin phantom, the membrane was first secured in customized clamps attached to a milling vise to form a translation stage and then brought level with a nominal applied load to define the baseline position. Images were taken by a commercial web camera (Logitech QuickCam Pro 4000, 960 x 1280 pixel resolution) that was rigidly mounted above the membrane at a single location to ensure a fixed field of view and frame of reference for the duration of the experiment. A series of five total images was collected (eight-bit grayscale) via laptop control of the camera—the baseline predeformation position and four subsequent positions with incremental stretches of approximately 5 mm each. Figure 4

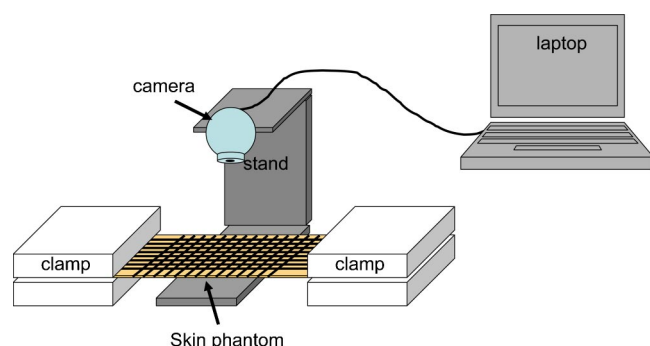


FIG. 4. An illustration of the skin-phantom setup for image acquisition.

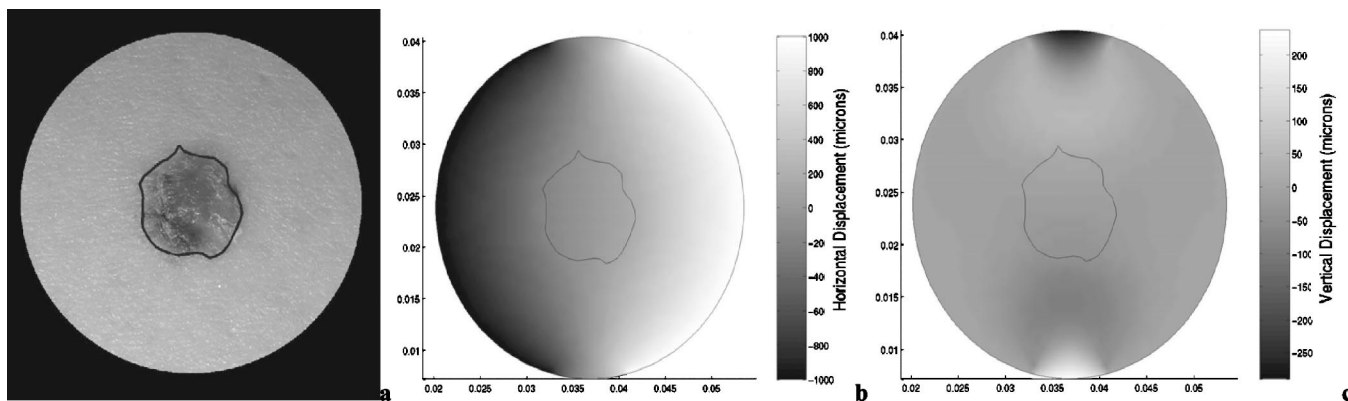


FIG. 5. (a) Melanoma lesion, reproduced with the permission of Dr. Lehmann, M.D., © Dermatlas, www.dermatlas.org, melanoma_1_040510. (b) Simulated horizontal and (c) vertical displacements shown (axis references are in meters while the gray scale is in microns). It should be noted that the contained region within the border represents the spatial regions of stiffness in this simulation and was not contained within image data provided to the MIE algorithm.

is a schematic of the experimental setup, while Fig. 3(a)–3(e) shows an example dataset.

E. Material testing protocol

Material testing was performed in order to determine the accuracy of the reconstructed Young's modulus values. When the phantoms were poured, specimens of both the bulk and stiff polyurethane were allowed to cure in separate containers from the membranes. These samples were then cut into $1\text{ cm} \times 1\text{ cm} \times 1\text{ cm}$ cubes. Compression testing was performed on an EnduraTEC ELF 3200 material tester (EnduraTEC Systems Group, Minnetonka, MN). The polyurethane was assumed to be elastic, homogenous, and isotropic.

The Enduratec material testing protocol involved ramping the actuator linearly from the zero position to 24% strain at 2% strain increments. The max strain value was chosen to extend slightly beyond the range of observed strain in the experiment shown in Fig. 3 which was approximately 22% strain for the bulk material. Although the stiffer inclusion material only experienced approximately 1%–2% strain, stress values were reported for the full strain range up to 24%. Between each change in axial position a three second dwell time was imposed to allow viscoelastic responses to subside. Stress–strain plots were produced for both the bulk material and the inclusion material. Three samples of each material were tested and an average curve was calculated.

F. Phantom experiment

To quantitatively test the MIE method within the context of dermoscopic applications using optical images, a series of studies using the elastic membrane of Fig. 3 were employed within the setup of Fig. 4. The single inclusion phantom was considered to be representative of a single lesion on the skin surface (nonpigmented in this case). The multiresolution MIE technique was used at each successive deformation for a total of four elasticity image reconstructions per similarity metric (in this case CC and GC only). The computational domain for these calculations involved 1051 nodes and 1973 elements. Boundary conditions were generated by analyzing

the pre- and post-deformed structured grid and estimating the domain's deformation. The Young's modulus reconstructions were then compared to the elasticity values as generated from the material testing protocol. It should be noted that only Young's modulus contrast was compared in these evaluations. This is due to the manner in which boundary conditions are prescribed in the model system. Currently, the approach is driven by displacement boundary conditions (i.e., Dirichlet type) which consequently make the elastic model only sensitive to Young's modulus contrast. Without knowledge of an applied stress at the boundary or a prescribed material property within the domain, absolute properties cannot be determined. In addition, it must also be noted that the reconstructions were constrained to a region of the phantom that was smaller than the overall phantom. This was a result from observing that at higher stretch states, out-of-plane distortions of the membrane became more prominent in the periphery.

G. Simulation experiments

In an effort to test the algorithm within the context of a more realistic image acquisition scenario for skin cancer, a simulation study was performed on an image of the 1 cm melanoma lesion shown in Fig. 5(a). In addition, a grid structure was not specifically applied to the lesion image so as to test whether the natural skin-texture itself contained sufficient image information for reconstruction. The lesion was provided by the Dermatology Image Atlas project (www.dermatlas.org, Image Name: melanoma_1_040510, Contributed by Eric Ehrsam, M.D.) and represents a 1 cm pigmented melanoma plaque, located on the left arm of a 35-year-old woman.³⁸ For the simulation boundary conditions, an annulus-shaped mechanical stretching device was assumed which would systematically stretch two semicircular regions apart by 2 mm. The melanoma was assumed to have a 2:1 elasticity contrast level with normal tissue, i.e., the melanoma was twice as stiff as the surrounding skin. The computational domain for the inverse problem contained 1294 nodes and 2459 elements. In addition, the mesh used to generate the forward-problem data was approximately 10%

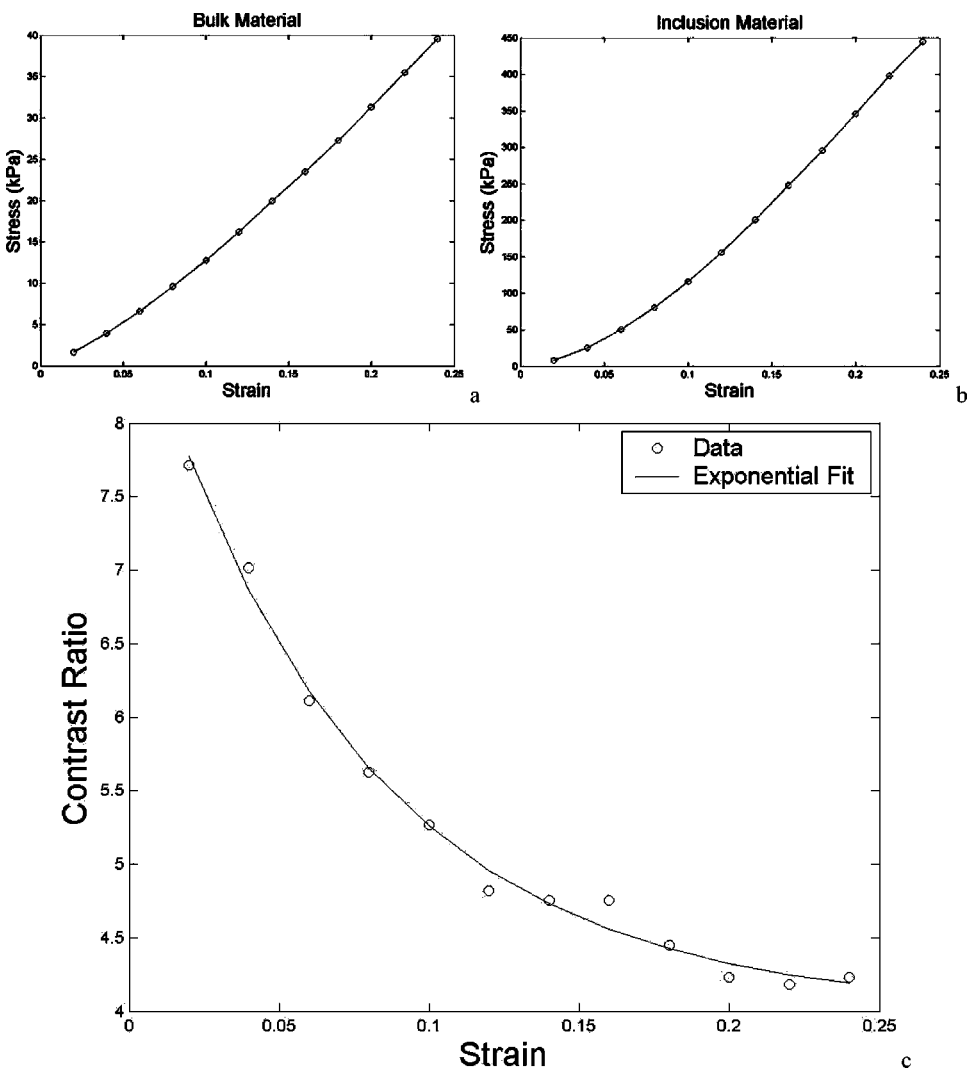


FIG. 6. (a) Stress versus strain behavior for bulk material, (b) stress versus strain behavior for inclusion material, and (c) inclusion-to-bulk contrast ratio at various levels of bulk material strain (for all ratio determinations, the inclusion's 2% strain value for Young's modulus was used which was the approximate maximum strain reached in the inclusion based on experiment observations).

more resolved than the mesh used for reconstruction. This introduced a small degree of variability to the boundary conditions and image deformation to simulate potential acquisition noise. Figure 5(b) and Fig. 5(c) illustrates the localized application of the stretching and the simulated solution for both horizontal and vertical displacements, respectively. Upon completion, these image data was used as input to the multiresolution MIE algorithm. Results are reported using the CC and GC image similarity methods.

III. RESULTS

A. Material testing

During the material testing phase, additional cyclic testing was performed in which viscoelastic behavior was noted. As a result, a waiting period was utilized at each strain level to allow viscoelastic responses to subside. The stress/strain behaviors at these quasistatic time periods for the bulk material and inclusion are shown in Figs. 6(a) and 6(b). In addition,

discrete finite difference approximations were made at the various strain levels to estimate a Young's modulus value. Table I represents a distribution of values calculated within the strain ranges tested. Once each modulus was calculated for each acquired strain level, a distribution of Young's modulus contrast ratios was calculated and is expressed by Eq. (2):

TABLE I. Young's elastic modulus values at several experimental strain levels.

Material strain (%)	Bulk material (kPa)	Inclusion material (kPa)
2	112.5	868.0
8	154.3	1635.0
12	180.0	2125.0
16	182.5	2375.0
23	206.3	2412.5

TABLE II. Contrast ratios for each experimental strain level.

Bulk material strain	Contrast ratio
Stretch 1: 8%	5.7
Stretch 2: 12%	5.0
Stretch 3: 16%	4.6
Stretch 4: 23%	4.2

$$CR(\varepsilon_{bulk}) = \frac{E_{inc}|_{\varepsilon=0.02}}{\bar{E}_{bulk}}, \quad (8)$$

whereby the inclusion's 2% strain value (approximate maximum strain reached in the inclusion based on experimental observations) for Young's modulus was used and the bulk material was allowed to vary over the entire strain range. This contrast ratio formulation reflects the reality of the membrane experiments shown in Fig. 3 whereby the soft surrounding material experienced the majority of deformation with the inclusion remaining relatively unchanged over all applications of stretch. The distribution of the contrast ratios as described by Eq. (8) at differing strain levels is shown in Fig. 6(c).

To assist in determining inclusion-to-bulk contrast ratios for different bulk strain levels in each experimental stretch as reflected in Fig. 3, an exponential curve fit was prescribed:

$$CR(\varepsilon = \varepsilon_{bulk}) = A + Be^{-C\varepsilon}, \quad (9)$$

whereby $A=4.0$, $B=5.0$, $C=13.8$. The root mean square contrast ratio error between model and acquired data over the entire acquired strain range was 0.093. The quality of the exponential model can be seen in Fig. 6(c). Using the expression described in (9), a series of Young's modulus contrast ratios values could be tabulated as a function of the specific strain levels used within the experiments of Fig. 1. These levels were determined by manually measuring strain levels within regions of the bulk material from the optical images. Table II reports the approximate contrast ratio for Young's modulus at the various bulk material strain levels experienced during the stretching experiments using Eq. (9).

B. Multiresolution MIE phantom reconstructions

Figures 7 and 8 are representations of the multiresolution elasticity image reconstruction performance for each of the different stretch states shown in Fig. 3 using CC and GC as the basis for image similarity, respectively. The boundary

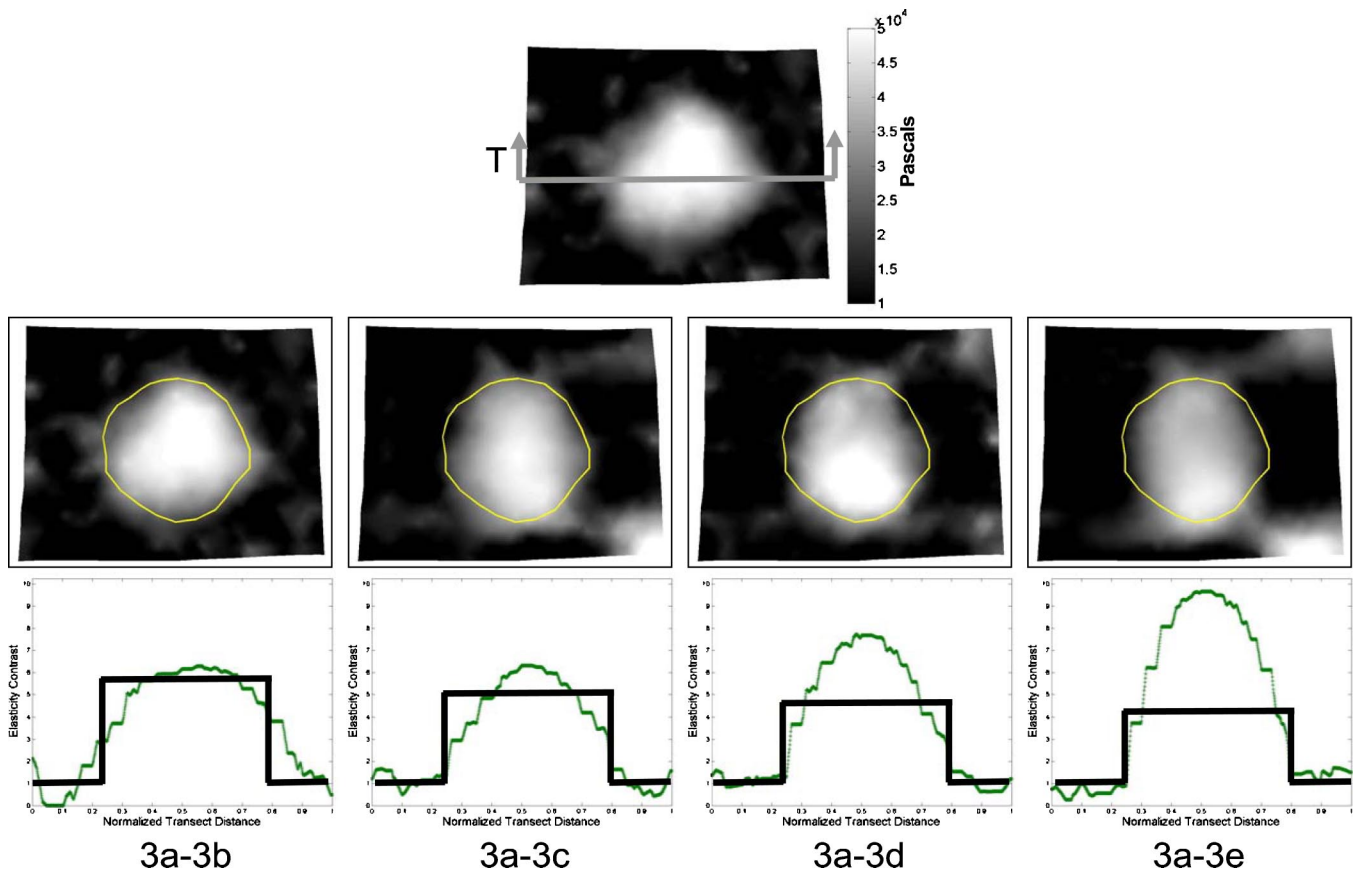


FIG. 7. An illustration of elasticity image reconstructions using CC where each column represents the respective stretch relative to Fig. 3 (e.g., 3a-3b represents the stretch from base to the first increment). The top image shows the location of a transect as designated by the T and the gray scale associated with Young's Modulus (Pa). The middle row represents the reconstructed elasticity images at each stretch state with the contour showing the actual inclusion location. The bottom row shows the elastic property contrast ratio as compared to that predicted with the material testing (shown as dark box-like contour) along the transect T.

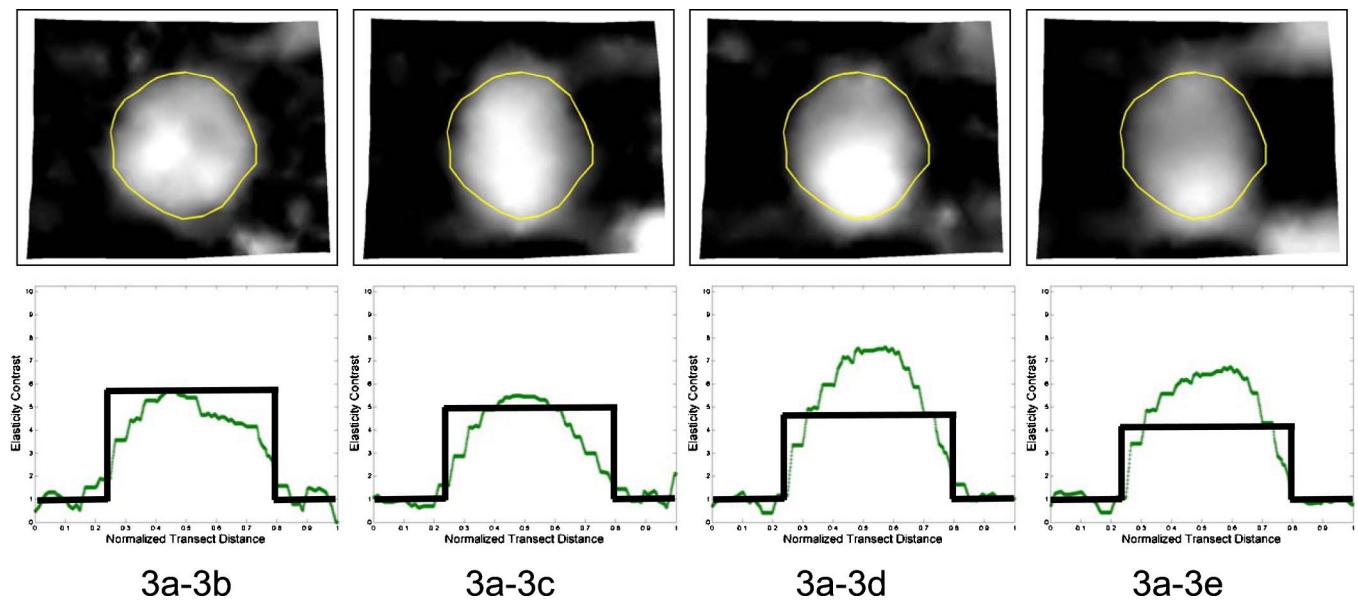


FIG. 8. Illustration of elasticity image reconstructions using GC where each column represents the respective stretch relative to Fig. 3 (e.g., 3a-3b represents the stretch from the base to the first increment). The top row represents the reconstructed elasticity images at each stretch state. The bottom row shows the elastic property contrast ratio as compared to that predicted with material testing (shown as a dark box-like contour) along the transect T which was designated in Fig. 7.

contour represents the inclusion location as shown within the image. The contrast ratios designated within the transect images of Figs. 7 and 8 were based on Table II.

Figure 9 shows elasticity images at varying stage resolutions within the multiresolution MIE reconstruction (reconstruction shown is the GC-3a-3b stretch regime).

To test the effect of the multiresolution framework, the same optical images were provided to our algorithm using a 400 property *region* resolution with an initial guess of homogeneity (i.e., coarser resolution solutions were not used as initial guesses). In results not reported here, the CC reconstruction was able to localize and quantify the stiff region similar to that of Fig. 7 at the high stretch states but was much worse with respect to the initial stretch state (i.e., 3a-3b image reconstruction).

Figure 10 represents the GC result for the four stretch states using the single 400 *region* high resolution parametrization. In Fig. 10(a) (3a-3b stretch state), the inclusion is

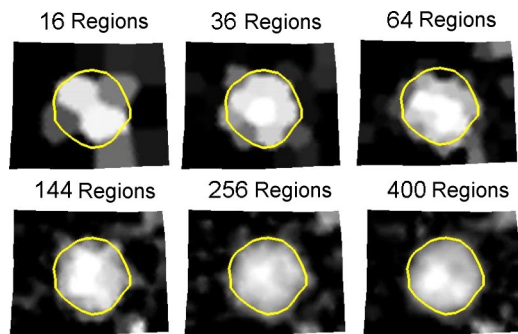


FIG. 9. Elasticity image reconstruction for the GC 3a-3b reconstruction case at various resolutions of the multiresolution algorithm. The gray scale is the same as in Fig. 7.

localized but the contrast resolution is poor compared with its multiresolution counterpart in Fig. 8, first column. At subsequent stretch states (3a-3c, 3a-3d, and 3a-3e), the elasticity image has not converged to an acceptable representation of the inclusion. Interestingly, the distance traveled by grid squares within the homogenous regions near the stretching edge within the second stretch state (3a-3c) is approximately the size of one grid square (~ 1 cm).

It is evident that by using a single high resolution parametrization as opposed to a multiresolution approach, a local minimum is found and the elasticity image degrades considerably. Consequently, the error magnitude for the image shown in Fig. 8, the second column is a factor of 50% smaller than that of Fig. 10(b) thus demonstrating that Fig. 10(b) indeed represents a local minimum (it should be noted that all parameters were identical—number of similarity zones, filtering, regularization, relaxation, etc.).

C. Multiresolution MIE melanoma reconstruction simulations

In addition to the experimental results shown above, several similar simulations were executed using a pigmented melanoma image. Figure 11 shows the elasticity image reconstruction and transect results using the multiresolution MIE framework for both CC and GC. Figure 12 illustrates the inter-resolution results from the GC reconstruction shown in Fig. 11.

IV. DISCUSSION

The elasticity image results from phantom (Figs. 7–9) and simulation (Figs. 11 and 12) studies demonstrate the utility of the multiresolution MIE approach. In addition, comparing

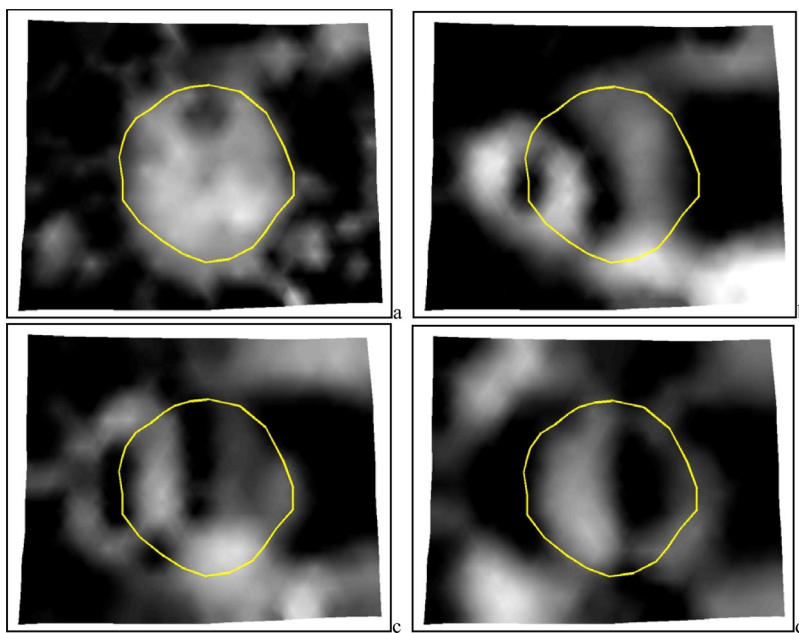


FIG. 10. GC reconstructions using single 400 property zone resolution for (a) 3a–3b, (b) 3a–3c, (c) 3a–3d, and (d) 3a–3e, respectively. The gray scale is the same as in Fig. 7.

the results in Figs. 8 and 10 clearly illustrates that instances can exist in which a single-resolution approach will fail whereas the multiresolution succeeds. A separate but related concern which is still under investigation is the degree and content of the image pattern needed to facilitate reconstruction; however, the preliminary elasticity image results from the melanoma simulations reported herein suggest that a sufficient intensity content exists in standard dermoscopic images.

Another important advance in this paper over previous work is the comparison between reconstructed elastic properties and their separately measured counterparts. The stress-strain curves shown in Figs. 6(a) and 6(b) and modulus values in Table I demonstrate a nonlinear elastic behavior. A good representative exponential fit to the Young's modulus contrast ratio data was achieved in Fig. 6(c) and provides a direct comparison to MIE-derived Young's modulus properties. One shortcoming is that because MIE is completely driven by displacement boundary conditions, only the contrast in Young's modulus values can be compared. However, the goal within this work is to investigate elastic properties as a mechanism for contrast within medical images.

Overall, the elastic image reconstructions shown in Figs. 7 and 8 demonstrated good localization with a varied performance in maintaining lesion shape integrity for both the CC and GC similarity methods, respectively. It appears that at high strain levels, MIE was less successful at capturing the anticipated contrast ratio. In fact, in both CC and GC, the ratio was overestimated, thus producing more contrast. It should be noted that the reconstructions shown were performed on a domain that represented only a portion of the image that surrounded the inclusions ($\sim 3\text{--}4$ cm from the inclusion border). This was due to our inability to completely control the physical boundaries of the phantom given the large mismatch between the stiffness values of the two materials. This manifested itself as out-of-plane warping of the

phantoms, i.e., a wrinkling at edges as the strain on the skin phantoms increased. The spatial location of these membrane distortions was more prominent with the distance from the inclusion. By making a more localized reconstruction region, the influence of these distortions was minimized although some effects are undoubtedly present. Ultimately, these out-of-plane motions would be interpreted as planar strains in the optical image acquisition system shown in Fig. 4. Although this variability in shape integrity existed, successful localization was achieved for all stretch states. It was encouraging that at small stretch states, where the model is most appropriate, proper quantitative contrast ratios were achieved (stretch states 3a–b, 3a–c in Figs. 7 and 8). Further encouragement was provided by successful localizations at high stretch states whereby nonlinear behavior is undoubtedly present and the small-strain assumptions are compromised (although the quantitative contrast ratio was not as satisfying). Undoubtedly, a large-deformation model is necessary at these higher strains to match contrast ratios at this level; however, if proper empirical characterizations could be done using the linear model over many stretch states, effective contrast thresholds could be determined for the characterization of lesions. In addition, these results were also promising in that successful Young's modulus contrast and localization was achieved with a nonpigmented lesion. This indicates that only the deflections of the surrounding image pattern and not the lesion image intensity itself are responsible for the changes in the elastic modulus values. This enthusiasm must be tempered by the realization, however, that the *in vivo* model may require more thought with respect to boundary conditions. Undoubtedly, the influence of subcutaneous tissue connectivity would influence the results here if these additional constraints were applied. Given the inherent link between the image formation and the validity of the computational model, more work needs to be performed prior to clinical deployment.

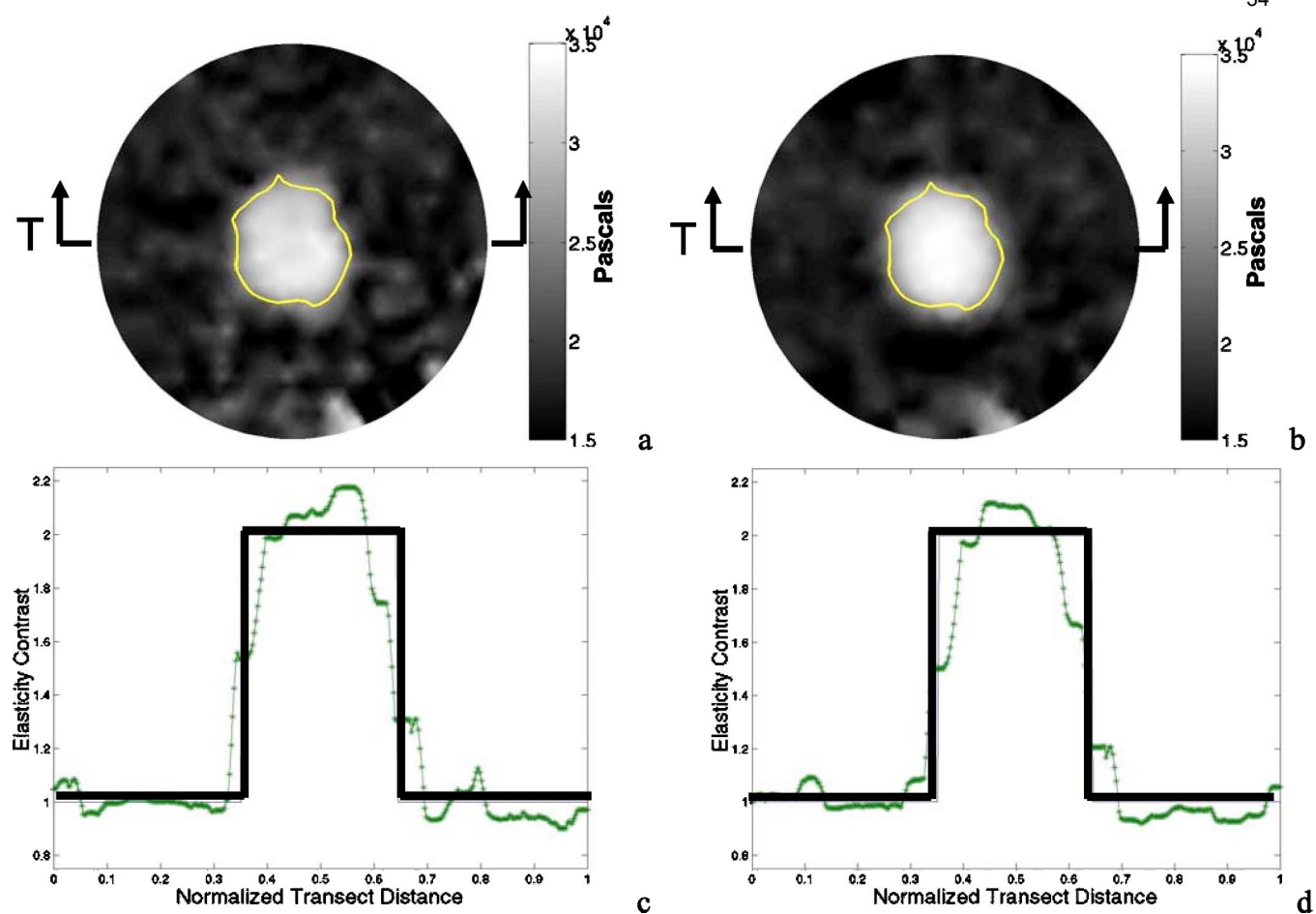


FIG. 11. Elasticity image reconstruction of melanoma using (a) CC and (b) GC with contrast ratio values along the transect for (c) CC and (d) GC, respectively. The location of transect is designated by the **T** shown in (a) and (b).

Although these results are encouraging, not all reconstructions exhibited the same peak modulus or lesion localization. One reason could be the accuracy to which boundary conditions were determined for each stretch state. It is possible that the manual delineation of boundary conditions or the observed wrinkling at high stretch states resulted in some boundaries being mapped less precisely than others. In some of the reconstructions, significant boundary artifacts can be observed. For example, in the second and fourth column of

Fig. 7, a Young's modulus peak is shown in the lower right hand region of the boundary. A second candidate for reconstruction inaccuracies across stretch states could be the degree of model-data mismatch. It is interesting to note the correlation between increased stretch and the marked decrease in accuracy of the contrast-ratio transect plots. At the smaller stretches, 3a-b and 3a-c, both CC and GC reconstructions perform better in both localization and quantification while both show overpredictions within transects for stretch states, 3a-d and 3a-e. A model-data mismatch would seem a likely source for this change in performance, considering that the elastic model used is a small-strain model and the levels of strain are less in the first two stretch states. One somewhat qualitative observation that can also be made is that the GC-based method appears to reconstruct somewhat better than the CC-based method. This is also the case within the melanoma simulations. Interestingly, in Ref. 30, a similar experience was found in that the GC method outperformed other methods with respect to our phantom reconstructions. The principal difference between the CC and GC similarity methods is the form of the image to be used when calculating the correlation coefficient. GC employs the edge map of the image while CC uses the raw acquired image. The increased performance by GC may indicate that areas of structured

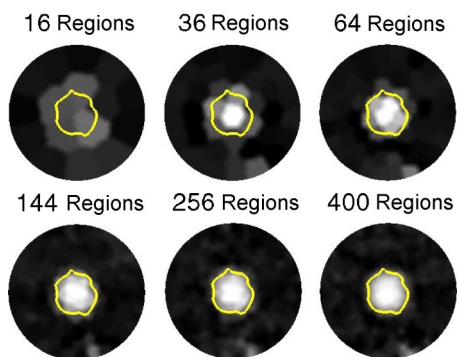


FIG. 12. An example of multi-resolution solution development using GC for melanoma simulation.

sharp gradient intensities influence the MIE approach more significantly than more gradual intensity changes. However, this statement must be tempered with the realization of Fig. 10 whereby structural decorrelation has occurred although arguably at much larger length scales as compared to those in traditional USE.

The results from the melanoma simulations provide a more realistic representation of the types of images that can be acquired within the clinic. These images provide their own challenge in that although the lesion is pigmented, the surrounding structured pattern of the grid used in the phantom was not present. In this case, it was desirable to test MIE without the presence of the structured grid. Overall, the elasticity images and transects were satisfying, with the GC qualitatively outperforming the CC method. One interesting observation is related to the apparent suppression of modulus noise within the GC elasticity image as compared to the CC. This is more than likely due to the suppression of low-frequency image characteristics associated with extracting edges within the source and target images.

Figures 9 and 12 demonstrate the multiresolution aspect to our approach by showing the reconstructions at all six resolutions used within the generation of our images. One beneficial aspect is the availability of intraresolution elasticity images which represent accurate, albeit coarse, assessments of image progression. In addition, these intraresolution images could be used to dynamically alter the *K*-means clustering approach to locally refine the reconstruction process for the next resolution (although not done in this study). This would alter the algorithm representation in Fig. 2 by replacing precomputed resolution maps with an internal process block which calculated *K*-means *regions* dynamically based on areas of interest found during the reconstruction process.

V. CONCLUSIONS

In this paper, a novel multiresolution extension to Modality Independent Elastography (MIE) has been implemented which simplifies previous work (a dual-grid technique) and is shown to be more robust than the single-resolution version. In addition, the multi-resolution architecture implemented facilitates the monitoring of reconstruction quality at intermediate resolutions. To test the approach, a membrane experimental setup was created which utilizes sets of optical images for the reconstruction process. The use of optical images to generate Young's modulus reconstructions does represent a new modality within MIE development and could potentially be used within dermoscopic applications.

Results from phantom and simulation experiments demonstrated that the multiresolution MIE approach is viable within the context for both nonpigmented and pigmented lesions, respectively. The nonpigmented phantom experiment highlighted direct comparisons between images of Young's modulus contrast and their independently measured counterparts, as provided by mechanical testing. Overall the results indicated good localization and quantification. However, results did indicate a dependence on the fidelity of the recon-

struction and the degree of applied deformation. In addition to the phantom experiment, a simulation using a clinical image of a pigmented melanoma were reported and illustrated excellent localization and quantification.

Despite potential limitations in elasticity image resolution when compared to traditional MRE and USE, MIE's adaptability to an optical image-registration platform at multiple scales is an intriguing possibility. Furthermore, this extension to another modality demonstrates that MIE-based approaches to elastography represent a new class of algorithms that may yield potentially new frameworks for disease characterization.

ACKNOWLEDGMENTS

This work was supported in part by the Whitaker Young Investigator Program, Whitaker Foundation, Arlington, VA. The authors would like to acknowledge the contribution of Chad W. Washington from the University of Mississippi, School of Medicine for his assistance in laboratory training of students involved in this work.

^{a)}Corresponding author.

- ¹American Cancer Society, "Cancer facts and figures 2004," July, 2004.
- ²A. A. Marghoob, L. D. Swindle, C. Z. M. Moricz, F. A. S. Negron, B. Slue, A. C. Halpern, and A. W. Kopf, "Instruments and new technologies for the *in vivo* diagnosis of melanoma," *J. Am. Acad. Dermatol.* **49**, 777–797 (2003).
- ³E. Ruocco, G. Argenziano, G. Pellacani, and S. Seidenari, "Noninvasive imaging of skin tumors," *Dermatol. Surg.* **30**, 301–310 (2004).
- ⁴R. Dua, D. G. Beetner, W. V. Stoecker, and D. C. Wunsch, "Detection of basal cell carcinoma using electrical impedance and neural networks," *IEEE Trans. Biomed. Eng.* **51**, 66–71 (2004).
- ⁵M. Gniadecka, P. A. Philipsen, S. Sigurdsson, S. Wessel, O. F. Nielsen, D. H. Christensen, J. Hercogova, K. Rossen, H. K. Thomsen, R. Gniadecka, L. K. Hansen, and H. C. Wulf, "Melanoma diagnosis by Raman spectroscopy and neural networks: Structure alterations in proteins and lipids in intact cancer tissue," *J. Invest. Dermatol.* **122**, 443–449 (2004).
- ⁶C. Edwards and R. Marks, "Evaluation of biomechanical properties of human skin," *Clin. Dermatol.* **13**, 375–380 (1995).
- ⁷L. J. Draaijers, Y. A. M. Botman, F. R. H. Tempelman, R. W. Kreis, E. Middelkoop, and P. P. M. van Zuijen, "Skin elasticity meter or subjective evaluation in scars: A reliability assessment," *Burns* **30**, 109–114 (2004).
- ⁸G. E. Pierard, C. Pierard-Franchimont, S. Vanderplaetsen, N. Franchimont, U. Gaspard, and M. Malaise, "Relationship between bone mass density and tensile strength of the skin in women," *Eur. J. Clin. Invest.* **31**, 731–735 (2001).
- ⁹G. E. Pierard, S. Vanderplaetsen, and C. Pierard-Franchimont, "Comparative effect of hormone replacement therapy on bone mass density and skin tensile properties," *Maturitas* **40**, 221–227 (2001).
- ¹⁰H. S. Yoon, S. H. Baik, and C. H. Oh, "Quantitative measurement of desquamation and skin elasticity in diabetic patients," *Skin Res. Technol.* **8**, 250–254 (2002).
- ¹¹C. Braham, D. Betea, C. Pierard-Franchimont, A. Beckers, and G. E. Pierard, "Skin tensile properties in patients treated for acromegaly," *Dermatology (Basel, Switz.)* **204**, 325–329 (2002).
- ¹²J. A. Clark, J. C. Y. Cheng, and K. S. Leung, "Mechanical properties of normal skin and hypertrophic scars," *Burns* **22**, 443–446 (1996).
- ¹³H. Dobrev, "In vivo study of skin mechanical properties in psoriasis vulgaris," *Acta Derm Venereol* **80**, 263–266 (2000).
- ¹⁴D. N. H. Enomoto, J. R. Mekkes, P. M. M. Bossuyt, R. Hoekzema, and J. D. Bos, "Quantification of cutaneous sclerosis with a skin elasticity meter in patients with generalized scleroderma," *J. Am. Acad. Dermatol.* **35**, 381–387 (1996).
- ¹⁵N. Nikkels Tassoudji, F. Henry, C. Pierard-Franchimont, and G. E. Pierard, "Computerized evaluation of skin stiffening in scleroderma," *Eur. J. Clin. Invest.* **26**, 457–460 (1996).

¹⁶H. Sumino, S. Ichikawa, M. Abe, Y. Endo, O. Ishikawa, and M. Kurabayashi, "Effects of aging, menopause, and hormone replacement therapy on forearm skin elasticity in women," *J. Am. Geriatr. Soc.* **52**, 945–949 (2004).

¹⁷J. Ophir, I. Cespedes, H. Ponnekanti, Y. Yazdi, and X. Li, "Elastography—A quantitative method for imaging the elasticity of biological tissues," *Ultrason. Imaging* **13**, 111–134 (1991).

¹⁸R. Muthupillai, D. J. Lomas, P. J. Rossman, J. F. Greenleaf, A. Manduca, and R. L. Ehman, "Magnetic-resonance elastography by direct visualization of propagating acoustic strain waves," *Science* **269**, 1854–1857 (1995).

¹⁹L. V. Tsap, D. B. Goldgof, and S. Sarkar, "Nonrigid motion analysis based on dynamic refinement of finite element models," *IEEE Trans. Pattern Anal. Mach. Intell.* **22**, 526–543 (2000).

²⁰L. V. Tsap, D. B. Goldgof, and S. Sarkar, "Fusion of physically-based registration and deformation modeling for nonrigid motion analysis," *IEEE Trans. Image Process.* **10**, 1659–1669 (2001).

²¹L. V. Tsap, D. B. Goldgof, S. Sarkar, and P. S. Powers, "A vision-based technique for objective assessment of burn scars," *IEEE Trans. Med. Imaging* **17**, 620–633 (1998).

²²J. L. Gennisson, T. Baldeweck, M. Tanter, S. Catheline, M. Fink, L. Sandrin, C. Cornillon, and B. Querleux, "Assessment of elastic parameters of human skin using dynamic elastography," *IEEE Trans. Ultrason. Ferroelectr. Freq. Control* **51**, 980–989 (2004).

²³M. I. Miga, "A new approach to elastography using mutual information and finite elements," *Phys. Med. Biol.* **48**, 467–480 (2003).

²⁴J. Ophir, S. K. Alam, B. Garra, F. Kallel, E. Konofagou, T. Krouskop, and T. Varghese, "Elastography: ultrasonic estimation and imaging of the elastic properties of tissues," *Proc. Inst. Mech. Eng., Part H: J. Eng. Med.* **213**, 203–233 (1999).

²⁵T. L. Chenevert, A. R. Skovoroda, M. O'Donnell, and S. Y. Emelianov, "Elasticity reconstructive imaging by means of stimulated echo MRI" *Magn. Reson. Med.* **39**, 482–490 (1998).

²⁶R. Sinkus, J. Lorenzen, D. Schrader, M. Lorenzen, M. Dargatz, and D. Holz, "High-resolution tensor MR elastography for breast tumour detection" *Phys. Med. Biol.* **45**, 1649–1664 (2000).

²⁷D. B. Plewes, J. Bishop, A. Samani, and J. Sciarretta, "Visualization and quantification of breast cancer biomechanical properties with magnetic resonance elastography" *Phys. Med. Biol.* **45**, 1591–1610 (2000).

²⁸E. E. W. Van Houten, M. I. Miga, J. B. Weaver, F. E. Kennedy, and K. D. Paulsen, "Three-dimensional subzone-based reconstruction algorithm for MR elastography" *Magn. Reson. Med.* **45**, 827–837 (2001).

²⁹M. M. Doyley, P. M. Meaney, and J. C. Bamber, "Evaluation of an iterative reconstruction method for quantitative elastography" *Phys. Med. Biol.* **45**, 1521–1540 (2000).

³⁰C. W. Washington and M. I. Miga, "Modality independent elastograph (MIE): A new approach to elasticity imaging" *IEEE Trans. Med. Imaging* (in press).

³¹A. P. Boresi, *Elasticity in Engineering Mechanics*, 2nd ed. (Wiley, New York, 2000).

³²L. Lapidus and G. F. Pinder, *Numerical Solution of Partial Differential Equations in Science and Engineering* (Wiley, New York, 1982).

³³G. K. Rohde, A. Aldroubi, and B. M. Dawant, "The adaptive bases algorithm for intensity based nonrigid image registration" *IEEE Trans. Med. Imaging* **22**, 1470–1479 (2003).

³⁴D. Rueckert, C. Hayes, C. Studholme, P. Summers, M. Leach, and D. J. Hawkes, "Non-rigid registration of breast MR images using mutual information," in *Medical Image Computing and Computer-Assisted Intervention — Miccai'98*, Lecture Notes in Computer Science, 1998, Vol. **1496**, pp. 1144–1152.

³⁵D. Rueckert, L. I. Sonoda, C. Hayes, D. L. G. Hill, M. O. Leach, and D. J. Hawkes, "Nonrigid registration using free-form deformations: Application to breast MR images," *IEEE Trans. Med. Imaging* **18**, pp. 712–721 (1999).

³⁶D. W. Marquardt, "An algorithm for least-squares estimation of nonlinear parameters," *SIAM J. Appl. Math.* **11**, 431–441 (1963).

³⁷N. Joachimowicz, C. Pichot, and J. P. Hugonin, "Inverse scattering: an iterative numerical method for electromagnetic imaging" *IEEE Trans. Biomed. Eng.* **39**, 1742–1752 (1991).

³⁸B. A. Cohen and C. U. Lehmann, "Dermatology Image Atlas" Dermatlas, 2000–2004.

³⁹T. L. Bialy, J. Whalen, E. Veledar, D. Lafreniere, J. Spiro, T. Chartier, and S. C. Chen, "Mohs micrographic surgery vs traditional surgical excision—A cost comparison analysis," *Arch. Dermatol.* **140**, 736–742 (2004).